A universal uptake mechanism for cobalt(II) on soil constituents: Ferrihydrite, kaolinite, humic acid, and organo-mineral composites

Gemma L. Woodward [a],*, Caroline L. Peacock [a],*, Alba Otero-Fariña [b], Olivia R. Thompson [c], Andrew P. Brown [d], Ian T. Burke [a],*

[a] School of Earth and Environment, University of Leeds, Leeds LS2 9JT, UK
[b] Department of Physical Chemistry, University of Santiago de Compostela, Avenida de las Ciencias s/n, 15782 Santiago de Compostela, Spain
[c] National Nuclear Laboratory Ltd., Chadwick House, Warrington, Cheshire WA3 6AE, UK
[d] School of Chemical and Process Engineering, University of Leeds, Leeds LS2 9JT, UK

Abstract

Cobalt is a waste product in many industrial processes and its most common radioactive isotope – ^{60}Co – is a by-product of nuclear reactors. To better understand the mobility and fate of Co in natural and contaminated environments we investigated Co sorption behaviour to the common soil and sediment constituents ferrihydrite, kaolinite, humic acid (HA), and ferrihydrite-HA and kaolinite-HA organo-mineral composites using sorption batch experiments, synchrotron X-ray absorption spectroscopy (EXAFS), and scanning transmission electron microscopy (STEM). We measured the sorption of Co to the end-member mineral and organic phases and the composites as a function of pH, ionic strength and Co concentration, and also for the composites as a function of organic carbon concentration, with composites made containing a wide range of organic carbon contents. We then determined the molecular mechanisms of Co sorption to the end-member phases and the composites, and used this information to develop molecularly constrained thermodynamic surface complexation models to quantify Co sorption. Sorption to the ferrihydrite-HA and kaolinite-HA organo-mineral composites was found to be inter-mediate to both of the end-member phases, displaying enhanced sorption respective to the mineral end-member phase at mid-low pH. EXAFS analysis shows that there is a universal sorption mechanism accounting for Co sorption to the end-member mineral and organic phases and the organo-mineral composites at mid-high pH, in which Co sorbs to these phases via inner-sphere bidentate binuclear surface complexes. At mid-low pH, sorption to all the phases except ferrihydrite is the result of outer-sphere complexation. Our new molecularly constrained thermodynamic surface complexation models for Co sorption to ferrihydrite, kaolinite, HA, and ferrihydrite-HA and kaolinite-HA organo-mineral composites, show that Co sorption to the composites cannot be modelled assuming linear additivity of Co sorption to the end-member phases.
© 2018 The Authors. Published by Elsevier Ltd. This is an open access article under the CC BY license (http://creativecommons.org/licenses/by/4.0/).

Keywords: Cobalt; Sorption; EXAFS; TEM; Iron (hydr)oxides; Kaolinite; Humic acid; Composites; Surface complexation model

1. INTRODUCTION

Cobalt can be released into the environment as a heavy metal from a variety of industrial sources, including coal power plants, vehicle emissions and through metal production (Gál et al., 2008), and as a radionuclide, most

* Corresponding authors.

E-mail addresses: ee11glw@leeds.ac.uk (G.L. Woodward), C.L.Peacock@leeds.ac.uk (C.L. Peacock), I.T.Burke@leeds.ac.uk (I.T. Burke).

commonly as ^{60}Co, present in the cooling water of nuclear reactors, or in radioactive waste, decaying via ionising gamma radiation with a half-life of ~5 years. Cobalt most commonly occurs in the environment as the Co^{2+} ion, which is highly soluble in water and so potentially very mobile. In low concentrations Co is an essential nutrient but too high concentrations can result in insufficient plant chlorophyll production and death (Hewitt, 1953). The potential environmental harm posed by both stable and radioactive isotopes of Co means that it is important to understand how Co interacts with soil constituents in order to predict Co mobility and fate and develop soil remediation methods.

Soils contain a complex mixture of components including primary and secondary minerals and organic materials in varying proportions, but it is interactions with relatively low abundance, high surface area phases such as iron (hyr) oxides, clays and humic substances that typically control the sorption behaviour, and thus the mobility, of many divalent metal cations in soils, including Co (Sparks, 1995). A common approach to understanding Co sorption behaviour has therefore been to study its sorption to separate mineral or organic phases (e.g., Ainsworth et al., 1994; Angove et al., 1998; Alvarez and Garrido, 2004). More recently, however, the sorption behaviour of metal cations in different physical mixtures and chemical composites of common soil minerals (such as kaolinite, Ka, and ferrihydrite, Fh) and organic materials has been investigated in an attempt to approach the complexity expected in natural soil environments (e.g., Zhu et al., 2010; Moon and Peacock, 2012, 2013; Otero Fariňa et al., 2018).

Macroscopic Co sorption behaviour to the iron (hydr) oxide Fh has been well documented (Forbes et al., 1976; Schenck et al., 1983; Ainsworth et al., 1994; Kanungo, 1994; Landry et al., 2009) with sorption occurring over a narrow pH range from ~5.5 to ~7 (Ainsworth et al., 1994; Landry et al., 2009) below which there is minimal to no sorption, and above which sorption reaches 100% of Co concentrations tested. In particular, Landry et al. (2009) reports no significant difference in sorption behaviour with changes in Co concentration and sorbate/sorbent ratio (with Co concentration from 10^{-4} to 10^{-6} mol L^{-1} and solid/solution from 2 to 5 g L^{-1}) or ionic strength (between 10^{-3} and 10^{-1} mol L^{-1} $NaNO_3$). On the other hand, Kanungo (1994) finds that increasing Co concentration from 4.1×10^{-5} to 2.0×10^{-4} mol L^{-1} does shift the sorption edge to higher pH values. In order to quantify the distribution of Co between the mineral and solution phases, Ainsworth et al. (1994) and Landry et al. (2009) fit the majority of their sorption data to a thermodynamic surface complexation model that invokes monodentate Co surface complexation to both strong and weak FeOH sorption sites. Despite these macroscopic observations and modeling inferences, however, there are no direct spectroscopic observations of Co sorption on any of the iron (hydr)oxides, and the local sorption environment of Co on Fh is still unconstrained.

Macroscopic Co sorption behaviour to the 1:1 phyllosilicate clay mineral Ka has also been studied extensively (Spark et al., 1995; Angove et al., 1998; Landry et al.,

2009). A two-stage sorption process is observed. In the first stage, sorption generally increases between pH 4 and 5.5 (Spark et al., 1995; Angove et al., 1998; Landry et al., 2009), then remains relatively stable between pH 5.5 and 6.5, and is highly dependent on ionic strength (Spark et al., 1995; Landry et al., 2009) with complete inhibition at 10^{-1} mol L^{-1} background electrolyte (Spark et al., 1995). Given the ionic strength dependence, this low pH sorption behaviour is attributed to complexation of Co^{2+} to the Ka siloxane faces until these sites become saturated (Spark et al., 1995; Angove et al., 1997; Angove et al., 1998) and it can be modelled by invoking non selective cation exchange involving permanent negative charge on the siloxane sites (Angove et al., 1998). This is consistent with spectroscopic data for Co sorption to Ka at low pH that indicates only outer-sphere sorption (O'Day et al., 1994a). In the second stage above pH ~ 6.5, sorption increases to 100% of the Co concentrations tested at pH ~ 8 (Spark et al., 1995; Angove et al., 1998; Landry et al., 2009) and is unaffected by changes in ionic strength or Co concentration (Landry et al., 2009). This behaviour is attributed to complexation of Co to the Ka amphoteric alumina faces (Schulthess and Huang, 1990). This is again consistent with spectroscopic data for Co sorption to Ka above pH ~ 6.5 which suggests that there are Al or Si backscattering atoms present at 2.7 ± 0.5 Å and 3.4 ± 0.05 Å, with the shorter of these bond lengths consistent with that predicted for inner-sphere bidentate Co complexes (Fig. 1) on the AlOH surface sites (O'Day et al., 1994a,b). Spectroscopic data also suggests that Co-Co second-neighbour atoms at 3.1 ± 0.02 Å become increasingly important with surface coverage (O'Day et al., 1994a,b) and this is interpreted as evidence for the formation of multinuclear surface complexes (O'Day et al., 1994a). Overall, Co sorption
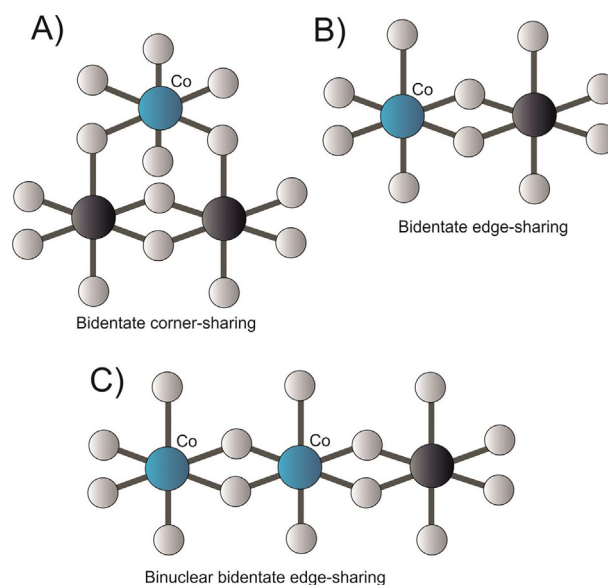

Fig. 1. Diagrams showing sorption mechanisms discussed in this study. Co atoms are labelled circles, unlabelled large circles are surface metal atoms of a standard mineral, and unlabelled smaller circles are oxygen atoms.

behaviour to Ka is generally modelled invoking outer-sphere cation exchange processes in combination with either inner-sphere monodentate or bidentate surface complexes (Angove et al., 1998; Landry et al., 2009).

While several previous studies focus on how Co sorbs to different soil constituents, including Fh at a macroscopic level and Ka at both macro- and microscopic levels, there has been almost no research to understand Co sorption behaviour in systems involving organo-mineral composites (Zachara et al., 1994). This is an important knowledge gap because contaminants do not react with soil phases in isolation, rather natural soil phases are present as more complex composites, where, for example, clays and iron (hydr)oxides are typically coated with organic matter in the form of humic substances and/or microbial cells (e.g., Davis, 1995; Sposito, 1984; Fortin and Langley, 2005). The purpose of this study is therefore to determine the mechanisms by which Co interacts with common soil constituents in the form of isolated end-member phases, Fh, Ka and humic acid (HA), and more complex organo-mineral composites of Fh-HA and Ka-HA, made by coating the pure mineral phases with sorbed HA. We investigate Co sorption as a function of pH, ionic strength and Co concentration, and also for the composites as a function of organic carbon concentration, with composites made containing a wide range of organic carbon contents. We determine the molecular sorption mechanisms of Co to the end-member mineral and organic phases and the composites using extended X-ray absorption fine structure (EXAFS) spectroscopy, and transmission electron microscopy (TEM) to visualise Co distribution at the nm-scale on the sorbent particles. Our work addresses the lack of underpinning spectroscopic information regarding the nature of Co sorption coordination with iron (hydr)oxides and humic substances, in comparison to that observed with Ka clay. From our analysis we develop molecularly constrained thermodynamic surface complexation models to investigate the nature of the Co sorption behaviour to the soil constituents, and in particular to determine whether Co sorption to the organo-mineral composites adheres to sorption additivity (i.e., can be predicted by assuming a simple mixture of phases).

2. METHODS

2.1. Materials

HA was obtained from an ombrotrophic peat soil in Galicia (NW Spain, 43°28′5.10″ N, 7°32′6.53″ W) (López et al., 2011). Preparation and characterization of the HA is reported in López et al. (2012). Briefly, the soil was acid-washed to remove inorganic components following Smith et al. (2004), and then HA was extracted following Swift (1996). Fh was synthesised as described in Schwertmann and Cornell (1991) by rapid hydrolysis of 0.1 M $Fe(NO_3)_3\cdot 9H_2O$ (aq) with 1 M NaOH at pH 7. After synthesis Fh was washed several times over a week in equivalent volumes of 18.2 MΩ cm MilliQ water, and subsequently stored as a slurry at 4 °C, following standard protocols to maintain mineralogical integrity

(Schwertmann and Cornell, 1991). Plastic labware and AR grade reagents were used throughout the Fh preparations. Mineralogically pure Ka (KGa-1b) was obtained from the Clay Minerals Society Source Clays Repository. Mineral identity and purity of the Fh and Ka was confirmed by X-ray powder diffraction (XRD) using a Bruker D8 Advance powder diffractometer and Cu–Kα radiation ($\lambda = 1.5406$ Å). The BET surface area of the end-member minerals was measured in triplicate using a Micrometrics Gemini VII 2390a using the N_2 sorption method after degassing for 16 h at room temperature. We report Fh and Ka surface areas of 295 ± 3 and 11.7 ± 0.1 m^2/g, respectively, which are in good agreement with literature values (Schwertmann and Cornell, 1991; Eick and Fendorf, 1998).

Three Fh-HA and two Ka-HA composites with different wt% adsorbed C were prepared following the method suggested by Iglesias et al. (2010). Briefly, 2 dry g equivalent of the pure mineral were suspended in 50 mL of 0.1 mol L^{-1} NaNO$_3$ and then mixed with a varying amounts of HA (23, 70, and 140 mL of 5.2 g L^{-1} HA slurry for Fh-HA composites, and 10 and 55 mL of 13.99 g L^{-1} HA slurry for Ka-HA composites) and DIW to make up a 500 mL solution. The pH was lowered to ∼4 by the addition of dilute HNO$_3$ to facilitate HA sorption and the solutions were agitated for 7 days. To wash the Fh-HA composites, the solutions were repeatedly mixed with equivalent volumes of DIW and centrifuged at 4000g for 10 min until the presence of HA in the supernatant was negligible, as determined by UV–Vis performed at 280 nm (Otero-Fariña et al., 2017). The Ka-HA composite particles were too fine for efficient centrifugation and were therefore washed via dialysis, using excess volumes of DIW and Membra-Cel MD44 14 × 100 CLR dialysis tubing with a 14 kDa cut off, until the electrical conductivity of the wash water equalled that of deionised water. All of the composites were stored as a slurry at 4 °C. The C content of the HA and composites was measured by combustion using a LECO SC-144DR Dual Range Sulfur and Carbon Analyzer 606-000. The three Fh-HA composites were found to have 5, 10, and 17 wt% C, and the Ka-HA composites had 1.4 and 2.2 wt% C.

2.2. Sorption experiments

Batch sorption experiments were carried out in 50 mL plastic centrifuge tubes at room temperature and in aerobic conditions. The pH range for the experiments was 3.5–8.4, representative of the pH of natural soils. 0.03 dry g equivalent weight samples (0.3 dry g equivalent for Ka) were mixed with 30 mL solutions of NaNO$_3$ (10^{-1}, 10^{-2}, or 10^{-3} mol L^{-1} NaNO$_3$) and Co so that the sorbents contained either 5.8, 0.58, or 0.058 wt% Co at 100% sorption (0.58, 0.058, or 0.0058 wt% Co for Ka). pH was recorded when there was less than 0.01 pH unit change in 15 s. Samples were adjusted to the chosen pH by dropwise addition of dilute NaOH or HNO$_3$. The samples were shaken continuously while the pH was monitored and set back to within ±0.15 of the desired pH. The pH values were then reset twice a day for 4 days until they remained constant for

16–24 h, after which time the experiments were concluded and the final pH was measured. The samples were centrifuged for 15 min at 3000g. The supernatant was filtered using 0.22 μm filters (10 kDa centrifuge filters in the case of the HA) and then 5 mL was added to 5 mL of 2% HNO_3 to maintain Co in solution. The Co concentration was determined (with an analytical uncertainty of $<\pm3\%$) on a Thermo iCAP 7400 radial ion-coupled plasma optical emission spectrometer (ICP-OES; ThermoFisher Scientific, USA).

PHREEQC (Parkhurst and Appelo, 1999) was used to calculate Co speciation in solution using the MINTEQ.V4 database (Charlton and Parkhurst, 2002) and is shown in Fig. S1 as a function of pH. Up to pH $\sim$ 8.5, Co^{2+} (aq) dominates Co speciation. At pH 8.3 $Co(OH)_2$ (s) begins to precipitate and by pH 8.5 it accounts for 50% of the Co total. Therefore in our experiments Co(II) is predominantly present as Co^{2+} (aq) throughout the pH range examined.

Supplementary data associated with this article can be found, in the online version, at https://doi.org/10.1016/j.gca.2018.06.035.

2.3. EXAFS spectra collection and data analysis

EXAFS spectra were collected at the Co K-edge (7722 eV) at Beamline B18 at Diamond Light Source Ltd, UK, operating at 3 GeV with a typical current of 300 mA. The X-rays at B18 are generated from a bending magnet source. The beam is vertically collimated by a Si mirror before passing through a double crystal Si monochromator. It was then focused onto the sample to give a spot size of 200×250 μm at the sample. Dried (40 °C) sorption samples were presented to the beam as 8 mm pressed pellets using cellulose as a dilutant to reduce chemical thickness. The sample pellets were held in Kapton™ tape for analysis, and a separate 1000 mg L^{-1} Co(NO$_3$) solution was also prepared and held in a polythene bag for analysis. Spectra were collected for the samples containing Ka and HA in fluorescence mode at room temperature ($\sim$295 °K) using a 32 element solid state Ge detector, and for the samples containing Fh in transmission mode at room temperature. Multiple scans were averaged to improve the signal to noise ratio and background subtracted using Athena version 0.9.25 from the Demeter package (Ravel and Newville, 2005). The resultant EXAFS spectra were then fit *ab initio* to model spectra produced by including a series of theoretical single and multiple scattering pathways calculated in Artemis version 0.9.25 (also from the Demeter package). Data were fit in a shell-by-shell manner to construct a structurally realistic best possible fit. Fit quality was assessed using the EXAFS R-factor and the reduced χ^2 function, which were calculated in Artemis for each model fit (the final best fit is reported in Tables 1 and 2). A fit is deemed to be of acceptable quality when the R-factor is less than or equal to 0.02 (Ravel and Newville, 2005). The reduced Chi^2 value allows comparison of fits with different parameterisation and therefore is only useful when comparing between samples or model fits and does not have its own ideal value. Additional longer backscattering pathways were only included if there was a >10% reduction in the reduced χ^2 function measure of goodness of fit. Uncertainties in the fitting parameters for each pathway (r, E0, S_0^2, and σ^2) were calculated individually and are also shown in Tables 1 and 2. For the EXAFS models of the composite samples, fits to individual end-member samples were combined and adjusted, if necessary, to produce an acceptable fit.

2.4. Scanning transition electron microscopy

Separate Fh, Ka and HA samples with Co surface loadings of approximately 1 wt% were prepared for (S)TEM analysis in the same way as the sorption experiments. Briefly 0.03 dry g equivalent of sorbent was suspended in 29.5 mL of 10^{-3} mol L^{-1} NaNO$_3$ and 0.6 mL 0.01 mol L^{-1} Co^{2+}. After 16 hrs the final pH was 7.5 ± 0.5; consistent with >90% aqueous Co removal in previous batch sorption experiments. Samples were then dispersed in methanol (or DI water in the case of HA) and a drop was pipetted onto a lacy/holey thin-film across a copper grid using a glass Pasteur pipette. As DI water was used to disperse the HA sample, the carbon film and grid underwent plasma treatment in a Fischione 1020 plasma cleaner for 10 s to make the film hydrophilic and ensure the sample was evenly distributed. (S)TEM images, energy dispersive X-ray (EDX) microanalysis elemental maps and electron energy loss spectra (EELS) were collected on an FEI Titan^3 Themis 300: X-FEG 300 kV S/TEM. This was fitted with S-TWIN objective lens, monochromator (energy spread 1.1 eV when the monochromator is de-excited), multiple high-angle annular dark-field (HAADF), annular dark-field (ADF), bright-field (BF) STEM detectors, FEI Super-X 4-detector EDX system, Gatan Quantum ER 965 energy filter for EELS and energy filtered TEM and Gatan OneView 4 K CMOS digital camera. To minimise potential sample damage (which was most important for Ka samples) a low beam current of 0.3 nA was used throughout data acquisition and limited magnification (280 k x) BF TEM imaging with short acquisition times (<1 s) was performed before commencement of HAADF STEM imaging and EDX elemental mapping (using a $\sim$80 pA probe current).

2.5. Surface complexation modeling

The sorption behaviour of Co on end-member Fh, Ka and HA and the organo-mineral composites was fit to a thermodynamic surface complexation model using the program EQLFOR (Sherman et al., 2008; Sherman, 2009). The Fh and Ka models were then combined with the HA model using a linear component additivity approach to explore Co sorption behaviour on the Fh and Ka organo-mineral composites. The surface electrostatics in all the models were accounted for by adopting the basic Stern model (BSM). The Davies equation was used for activity corrections to the stability constants for aqueous species. Detailed discussion on the development of the end-member Fh model is available in Moon and Peacock (2013), and for the Ka,

Table 1
Co K-edge EXAFS fitting parameters for Fh, Ka and HA samples, where N is the coordination number ($\pm25\%$), r is the interatomic distance, σ^2 is the Debye–Waller Factor and reduced χ^2 and R are the goodness of fit parameters. Uncertainties in the last digit shown in parentheses. MS = multiple scattering pathways within the CoO_6 octahedral and Co-O-Co linkages. MS pathways are italicised and do not contribute to the structural fit.

Experiment description	Pathway	N	r (Å)	σ^2 (Å^2)	χ^2; R
A: Co (aq) Standard	Co-O	6	2.07(1)	0.005(1)	771; 0.019
$\delta e0 = -3(1)$	*CoO$_6$ MS*	*12*	*4.14(2)*	*0.011(2)*	
$S_0^2 = 0.92$					
B: Fh_2wt%Co_0.1_pH8	Co-O	6	2.06(1)	0.011(1)	120; 0.013
$\delta e0 = -2(1)$	Co-Fe	1.3(3)	2.99(2)	0.006(3)	
$S_0^2 = 0.92$	Co-Co	1.6(4)	3.14(1)	0.005(2)	
	CoO$_6$ MS	*12*	*4.12(2)*	*0.022(2)*	
	Co-O-Co MS	*6(2)*	*3.66(1)*	*0.008(2)*	
C: Fh_2wt%Co_0.1_pH7	Co-O	6	2.04(1)	0.011(1)	288; 0.045
$\delta e0 = -3(2)$	Co-Fe	1.3(3)	2.99(3)	0.006(5)	
$S_0^2 = 0.92$	Co-Co	1.8(4)	3.14(3)	0.007(4)	
	CoO$_6$ MS	*12*	*4.09(2)*	*0.022(2)*	
	Co-O-Co MS	*6(2)*	*3.65(2)*	*0.009(3)*	
D: Fh_1wt%Co_0.1_pH8	Co-O	6	2.04(1)	0.009(1)	266; 0.022
$\delta e0 = -3(1)$	Co-Fe	1.1(3)	3.00(4)	0.006(7)	
$S_0^2 = 0.92$	Co-Co	1.7(4)	3.13(3)	0.007(4)	
	CoO$_6$ MS	*12*	*4.09(2)*	*0.018(2)*	
	Co-O-Co MS	*6(2)*	*3.65(2)*	*0.007(3)*	
E: Ka_1wt%Co_0.001_pH8	Co-O	6	2.06(1)	0.009(1)	121; 0.017
$\delta e0 = -3(1)$	Co-Al	0.5(1)	2.97(10)	0.014(17)	
$S_0^2 = 0.92$	Co-Co	1.2(3)	3.11(1)	0.004(1)	
	CoO$_6$ MS	*12*	*4.13(2)*	*0.018(2)*	
	Co-O-Co MS	*4(1)*	*3.64(1)*	*0.006(1)*	
F: Ka_1wt%Co_0.001_pH6	Co-O	6	2.07(1)	0.006(1)	445; 0.013
$\delta e0 = -2(1)$	*CoO$_6$ MS*	*12*	*4.14(2)*	*0.013(2)*	
$S_0^2 = 0.92$					
G: Ka_1wt%Co_0.001_pH5	Co-O	6	2.06(1)	0.007(1)	775; 0.015
$\delta e0 = -2(1)$	*CoO$_6$ MS*	*12*	*4.13(2)*	*0.014(2)*	
$S_0^2 = 0.92$					
H: HA_1wt%Co_0.1_pH8	Co-O	6	2.04(1)	0.010(1)	36; 0.006
$\delta e0 = 0(1)$	Co-C	2.3(5)	2.92(2)	0.006(4)	
$S_0^2 = 0.92$	Co-Co	0.9(2)	3.07(2)	0.007(2)	
	CoO$_6$ MS	*12*	*4.08(2)*	*0.020(2)*	
	Co-O-Co MS	*4(1)*	*3.61(2)*	*0.008(2)*	
I: HA_1wt%Co_0.1_pH4.6	Co-O	6	2.05(1)	0.008(1)	1062; 0.024
$\delta e0 = -3(1)$	*CoO$_6$ MS*	*12*	*4.11(2)*	*0.017(2)*	
$S_0^2 = 0.92$					
J: HA_1wt%Co_0.1_pH4	Co-O	6	2.05(1)	0.007(1)	642; 0.017
$\delta e0 = -3(1)$					
$S_0^2 = 0.92$					

HA and organo-mineral composite models in Section 4.3 below.

3. RESULTS

3.1. Co sorption to end-member ferrihydrite, kaolinite and humic acid

The results from pH sorption edge experiments using Fh, Ka, and HA are shown in Figs. 2 and 3 (n.b. only data from 0.58 wt% Co experiments is shown, where the solid:-solution ratio is 1 g L^{-1} in the Fh and HA experiments and 10 g L^{-1} in the Ka experiments; data from all Co^{2+} concentrations 0.058–5.8 wt% Co for the Fh and HA, and 0.0058–0.58 wt% Co for the Ka experiments are shown in SI Fig. S2).

For Fh we observe sigmoid sorption edges that are in agreement with previous studies of Co sorption onto iron (hydr)oxides (Forbes et al., 1976; Schenck et al., 1983; Ainsworth et al., 1994; Kanungo, 1994; Landry et al., 2009). There is no change in the shape or position of the sorption edges in pH space with increases in ionic strength

Table 2
Co K-edge EXAFS fitting parameters for Fh-HA and Ka-HA organo-mineral composite samples, where N is the coordination number ($\pm 25\%$), r is the interatomic distance, σ^2 is the Debye–Waller Factor and reduced χ^2 and R are the goodness of fit parameters. Uncertainties in the last digit shown in parentheses. MS = multiple scattering pathways within the CoO_6 octahedral and Co-O-Co linkages. MS pathways are italicised and do not contribute to the structural fit.

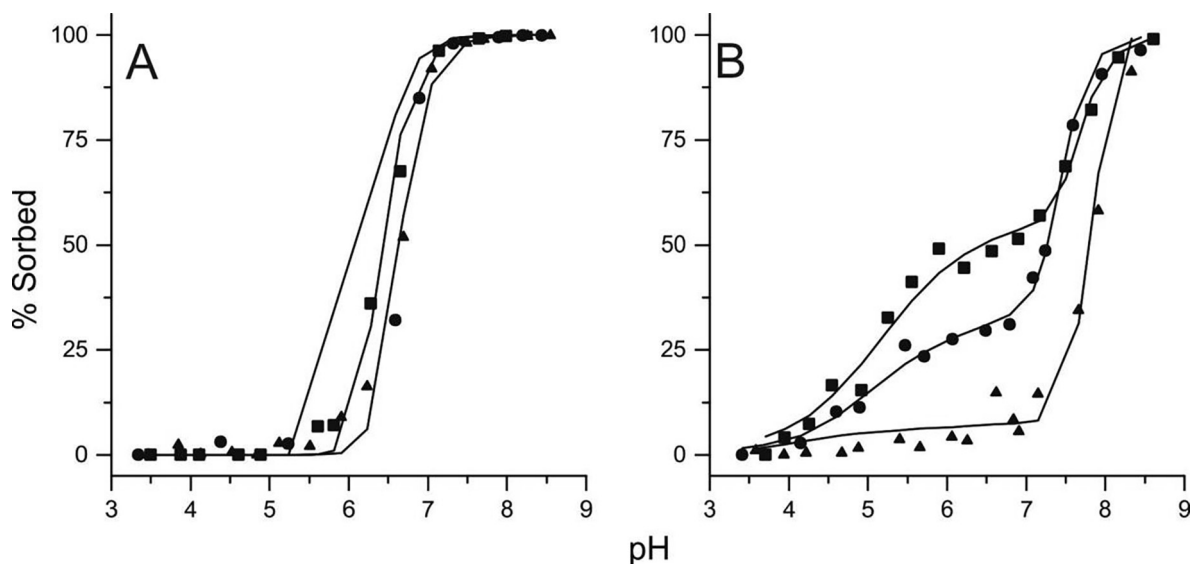| Experiment description	Pathway	N	r (Å)	σ^2 (Å^2)	χ^2; R
K: FhHA_2wt%Co_17wt%C_0.1_pH7	Co-O	6	2.05(1)	0.009(1)	90; 0.014
$\delta e0 = -3(1)$	Co-C	1.3(3)	2.95(12)	0.012(27)	
$S_0^2 = 0.92$	Co-Fe	0.6(2)	3.02(8)	0.007(13)	
	Co-Co	0.9(2)	3.17(5)	0.008(9)	
	CoO6 MS	*12*	*4.11(2)*	*0.018(2)*	
	Co-O-Co MS	*8(2)*	*3.67(3)*	*0.009(5)*	
L: FhHA_2wt%Co_17wt%C_0.1_pH6	Co-O	6	2.04(1)	0.007(1)	185; 0.025
$\delta e0 = -5(1)$					
$S_0^2 = 0.92$					
	CoO$_6$ MS	*12*	*4.09(2)*	*0.014(2)*	
M: KaHA_2.1wt%Co_2.2wt%C_0.001_pH8	Co-O	6	2.07(1)	0.009(1)	363; 0.031
$\delta e0 = -2(2)$	Co-C	2.5(6)	3.09(6)	0.011(12)	
$S_0^2 = 0.92$	Co-Co	1(2)	3.12(3)	0.007(4)	
	CoO$_6$ MS	*12*	*4.14(2)*	*0.019(2)*	
	Co-O-Co MS	*4(1)*	*3.65(2)*	*0.008(3)*	
N: KaHA_2.1wt%Co_2.2wt%C_0.001_pH6	Co-O	6	2.06(1)	0.006(1)	306; 0.013
$\delta e0 = -2(1)$	*CoO6 MS*	*12*	*4.12(2)*	*0.013(2)*	
$S_0^2 = 0.92$					
O: KaHA_2.1wt%Co_2.2wt%C_0.001_pH4	Co-O	6	2.06(1)	0.006(1)	279; 0.014
$\delta e0 = -3(1)$	*CoO$_6$ MS*	*12*	*4.13(2)*	*0.012(2)*	
$S_0^2 = 0.92$					

Fig. 2. Co sorption (at 10^{-4} mol L^{-1} Co total concentration, equating to 0.58 wt% Co sorbed at 100% sorption for Fh and 0.058 wt% Co sorbed at 100% sorption for Ka) to Fh (A) and Ka (B) as a function of pH; conducted at room temperature at a range of ionic strengths (10^{-3}, squares; 10^{-2}, circles; and 10^{-1}, triangles, mol L^{-1} NaNO$_3$). Solid lines are the surface complexation model fits for each system.

from 10^{-3} to 10^{-1} mol L^{-1} (Fig. 2) or with increases in Co concentration from 0.058 to 5.8 wt% Co (SI Fig. S2).

The Ka sorption edges show two sorption stages which is also in agreement with previous studies of Co sorption onto Ka (Spark et al., 1995; Angove et al., 1998; Landry et al., 2009). There is a decrease in the amount of Co sorbed during the initial sorption stage with increasing ionic strength from 10^{-3} to 10^{-1} mol L^{-1} (Fig. 2) The percentage
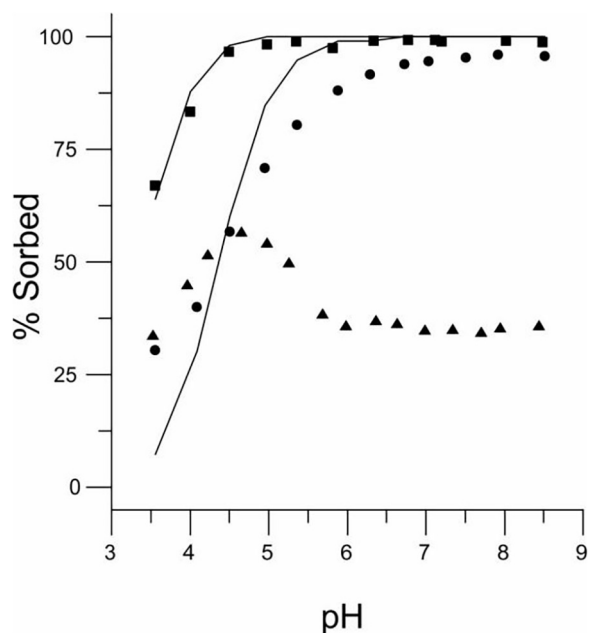
Fig. 3. Co sorption to HA at ionic strengths of 10^{-3} mol L^{-1} and 10^{-1} mol L^{-1}, and using two different filters before analysis (squares, 10^{-3} mol L^{-1} $NaNO_3$; circles, 10^{-1} mol L^{-1} $NaNO_3$ filtered with a 10 kDA centrifuge filter; triangles, 10^{-1} mol L^{-1} $NaNO_3$ filtered at 0.22 μm.) Solid lines represent the surface complexation model fits for each system.

of Co sorbed in the initial sorption stage also decreases when increasing the Co concentration from 0.0058 to 0.58 wt% Co (SI Fig. S2).

For HA we observe high sorption even at low pH values, which is consistent with previous studies of Co sorption on HA (McLaren et al., 1986). The sorption edge shifts to higher pH values when ionic strength is increased from 10^{-3} to 10^{-1} mol L^{-1} (Fig. 3). There is also a marked difference in sorption behaviour dependant on the filtration method used for equivalent samples. When the sample is filtered with a 10 kDa filter, sorption reaches 100%, however when it is filtered with a 0.22 μm filter, sorption peaks at ~60% and then decreases back down to ~35% where it remains stable (Fig. 3).

3.2. Co sorption to organo-mineral composites

The sorption of Co to the organo-mineral composites is plotted in Fig. 4 as a function of pH. The three Fh-HA composites show a generally sigmoidal shape, but the sorption edges are intermediate between those of the end-member Fh and HA, showing enhanced sorption relative to the end-member Fh in the mid-low pH regime. In particular at pH 3.5–5.5 there is negligible sorption to Fh, but the composites show 15–45% sorption. This is in good agreement with the sorption of other divalent cations to Fh organo-mineral composites (e.g., Zhu et al., 2010; Moon and Peacock, 2012, 2013).

The two Ka-HA sorption edges are also intermediate between those of the end-member Ka and HA, with the 1.4 wt% C composite edge falling below the end-member

Ka edge only above pH 7. The 1.4 wt% C and 2.2 wt% C composites show enhanced sorption relative to the end-member Ka in the low-mid pH regime and over the majority of the pH range studied, respectively.

3.3. EXAFS of end-member and composite phases

Spectra collected from all samples are fit with a series of single and corresponding multiple scattering pathways. The final best model fits are shown in Fig. 5 for all sample spectra and an aqueous Co standard solution, and the fit parameters are shown in Tables 1 and 2 for the end-member and composite systems, respectively. Additional Fh samples (with both very high and very low Co-loadings) that produced EXAFS spectra with high signal to noise ratio are presented in SI Table S1 and SI Fig. S3.

The amplitude reduction factor, S_0^2, determined for the fitting of all EXAFS samples was based on results obtained from the fitting of the EXAFS standard Co^{2+}(aq) solution. In this process, the CN (coordination number) of the Co-O path was set to 6 and the S_0^2 parameter fit to a value of 0.92. This value was used for all S_0^2 in all subsequent fits and models. The CN for the Co-O pathway was fixed at 6 for all samples, and we did not consider non-octahedrally coordinated Co^{2+}. For the sorption coordination we fit the CN's for the Co-Fe and Co-Co pathways iteratively to choose the best fit for the highest quality data. This was then applied to the lower quality data to ensure consistency. Given that the error on CN's is ~25% it was sensible to choose an intermediate number close to integer values for the subsequence fits.

The FEFF single scattering paths for the model were created from the basic atom coordinates of cobalt hydroxide, goethite, kaolinite, and Co-acetate, which account for Jahn-Teller distortions. A potential problem with this approach is that increasing the number of variables to be determined in the fitting minimization can make the uncertainties in the fitted variables intolerably large. However, the parameters for the MS paths (R, σ^2) can all be expanded quantitatively in terms of the single scattering paths that make up the individual legs of each of the multiple scattering paths. Thus the added multiple scattering paths do not need any additional variable parameters added to the fit and instead they add constraints to better define the single scattering paths, reducing the uncertainty of the first shell Co-O and Co-Co paths making such a fit attainable (Webb et al., 2005).

The spectra collected from the Co-sorbed Fh samples at all pH and Co concentrations are fit with the same molecular model, consisting of 6 O at ~2.05 Å, ~1 Fe at ~3 Å and ~1.5 Co at 3.1–3.2 Å. The Co-sorbed Ka spectra at low pH (pH 5 and 6) are fit with only 6 O at ~2.05 Å, similar to the $Co_{(aq)}$ standard, while at high pH (pH 8), the best fit model includes ~0.5 Al at ~2.9 Å and ~1 Co at ~3.1 Å. The Co-sorbed HA spectra at low pH (pH 4 and 4.6) are also fit with only 6 O, similar to the $Co_{(aq)}$ standard and the low pH sorption to Ka, while at high pH (pH 8) there are also ~2 C at ~2.9 Å and ~1 Co at ~3.1 Å. Co sorption to the Fh-HA composite spectrum at pH 6, is fit with 6 O at ~2.05 Å, ~1 Fe at ~3.02 Å and ~1.5 Co at ~3.2 Å, while at
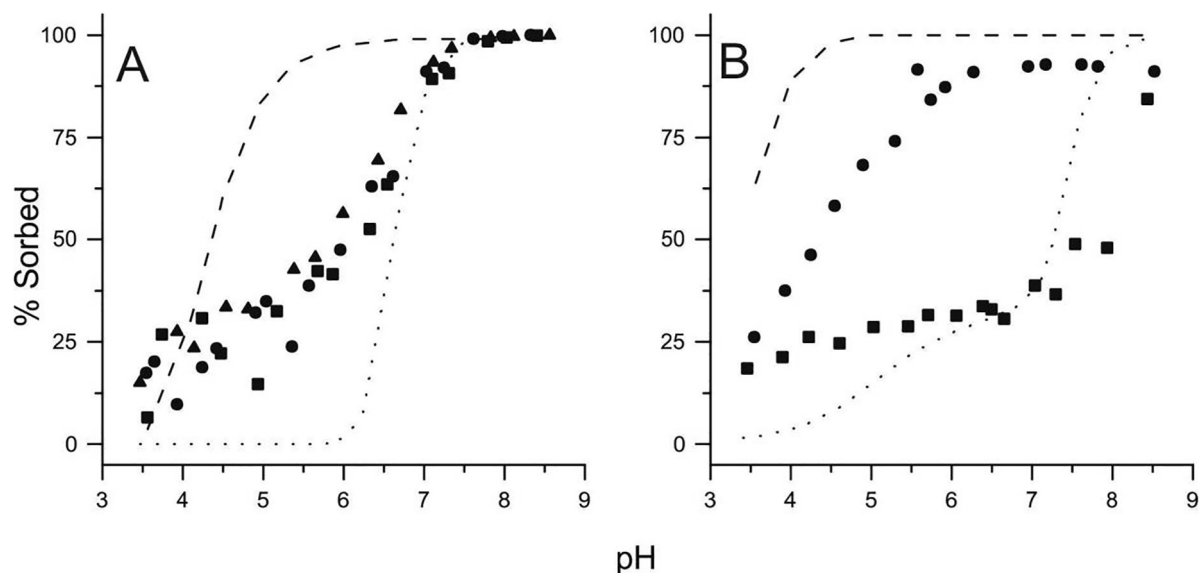
Fig. 4. Co sorption to Fh-HA (A) and Ka-HA (B) organo-mineral composites, both at a range of C contents (for the Fh-HA composites, squares show sorption to the composite with 5 wt% C; circles, 10 wt% C; and triangles, 17 wt% C; for the Ka-HA composites, squares show sorption to the composite with 1.4 wt% C, and circles 2.2 wt% C). In both graphs, the dashed line shows sorption to the HA end-member at the ionic strength of each experiment, and the dotted line shows sorption to the mineral end-member (Fh or Ka).

pH 7, the fit also includes ∼1 C at ∼2.9 Å. Sorption to the Ka-HA composite spectrum at pH 4 and 6 is fit with only 6 O at ∼2.05 Å, while at pH 8, there are also contributions from ∼2 C at ∼3.04 Å and ∼1 Co at ∼3.14 Å.

3.4. TEM imaging of Co-sorbed end-member ferrihydrite, kaolinite and humic acid

In low magnification imaging the Co-sorbed Fh sample is seen to consist of small (2–5 nm) particles that form much larger aggregates between 500 and 800 nm in size (Fig. 6). Relatively high magnification analysis of 5 areas of interest shows that none of these areas contain any nano-scale Co-containing particles. In all 5 areas of interest EDS mapping shows the Co to be homogenously distributed on the sample, though areas that are deemed to be thicker through observation of the HAADF image appear to have a higher concentration of Co (Fig. 6). Due to the possibility of overlap in the Fe K_β and Co K_α peaks in EDS analysis, the presence of Co associated with the Fh was confirmed using electron energy loss spectroscopy (EELS) and a distinct Co L_3-edge is detected at 780 eV.

In low magnification imaging the Co-sorbed Ka sample consists of hexagonal crystalline platelets between 100 and 400 nm in size with a depth of 10–50 nm (Fig. 7). Thirteen regions of interest were selected for relatively high magnification analysis, 2 imaging the planar platelet surface and the remainder imaging edge-on views of the crystals. No nano-scale Co-containing particles are observed in any region of interest. In EDS mapping Co is found to be heterogeneously distributed on the sample and in 5 regions of interest was detected specifically associated with the crystal edges. In these 5 regions, Co appears to be distributed such that it is found predominately on one face of each

crystal. In high resolution imaging these Co-rich faces appear to be regions where the Ka cleavage planes are rougher and less coherent than Co-free areas (Fig. 7).

In low magnification imaging the Co-sorbed HA sample consists of rounded amorphous particles displaying a very wide range of particle sizes (<100 nm to >2000 nm) (Fig. 8). Three areas of interest were studied at a high resolution and in all of these areas EDS mapping shows Co homogenously distributed on the sample with no nano-scale Co-containing particles (Fig. 8).

4. DISCUSSION

4.1. Co sorption to end-member ferrihydrite, kaolinite and humic acid

4.1.1. Co sorption to ferrihydrite

The sorption edge data for Fh (Fig. 2A and SI Fig. S1A) compares well with that reported in the literature for Co sorption to iron (hydr)oxides, with sorption edges in the range pH 6–7 (Ainsworth et al., 1994; Landry et al., 2009). The percentage of Co sorbed is independent of initial Co concentration (SI Fig. S1A), suggesting that in our sorption systems there is an excess of surface sorption sites, consistent with the large surface area for Fh (∼295 ± 3 m²/g). The Co sorption behaviour is also independent of ionic strength (Fig. 2A) suggesting that Co binds to Fh via inner-sphere surface complexation. This is confirmed by EXAFS analysis of Co sorbed to Fh at pH 7 and 8 as all samples are fit with 1 Fe at ∼3.0 Å (Table 1). The number of Fe backscatterers and the Co-Fe interatomic distance indicates that octahedral Co-O moieties form inner-sphere bidentate edge-sharing complexes with FeOH octahedral surface groups at the pH values investigated (e.g., for copper sorption to
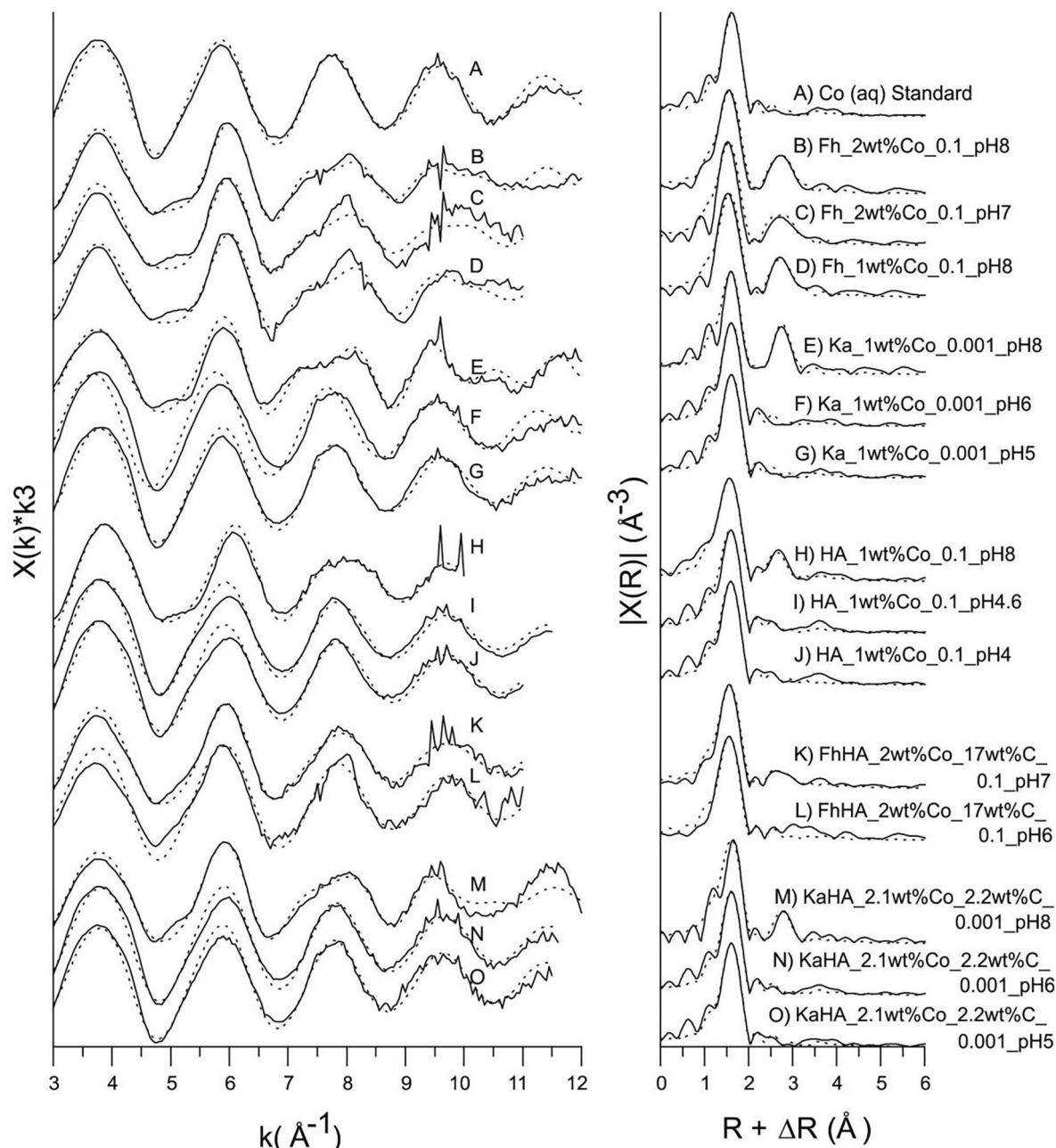
Fig. 5. EXAFS spectra and resulting Fourier transforms of each sample. Sample names are presented as: adsorbent_wt% Co_wt% C (only necessary for the composite phases)_ionic strength (in mol L^{-1}) and sample pH. The solid line represents the data and dotted line is the best fit. Samples showing signs of low signal:noise and self-absorption have been omitted, but are shown in SI Fig. S3.

Fh; Scheinost et al., 2001; Moon and Peacock, 2012; Otero Fariña et al., 2018). EXAFS data were also fit with ~1.5 Co at ~3.14 Å (Table 1) indicating the presence of Co hydroxide-like linkages as opposed to Co hydroxide surface precipitates in which the CN for the Co-Co pathway would be higher. As the Co-Co CN is between 1 and 2, it is possible that Co is forming a mixture of bi- and tri-nuclear surface complexes, as the CN will tend towards 2 as the chain length increases. Although Fe and Co are similar X-ray backscat-terers, the modelled Co-Fe and Co-Co pathways as

calculated in FEFF have sufficiently different distances (~0.1 Å) that they can be resolved in the EXAFS fit. Addition of both Co-Fe and Co-Co pathways improved the model fits despite also increasing the total degrees of freedom when compared to models with either Co-Fe or Co-Co. TEM observations (Fig. 6) however, show that even at relatively high Co loadings Co is evenly dispersed on the Fh surfaces and does not form discrete $Co(OH)_2$ nanoparticles. Furthermore, 1.5 Co-Co bonds is significantly below the 6 Co-Co bonds present in $Co(OH)_2$ (O'Day et al., 1994a).
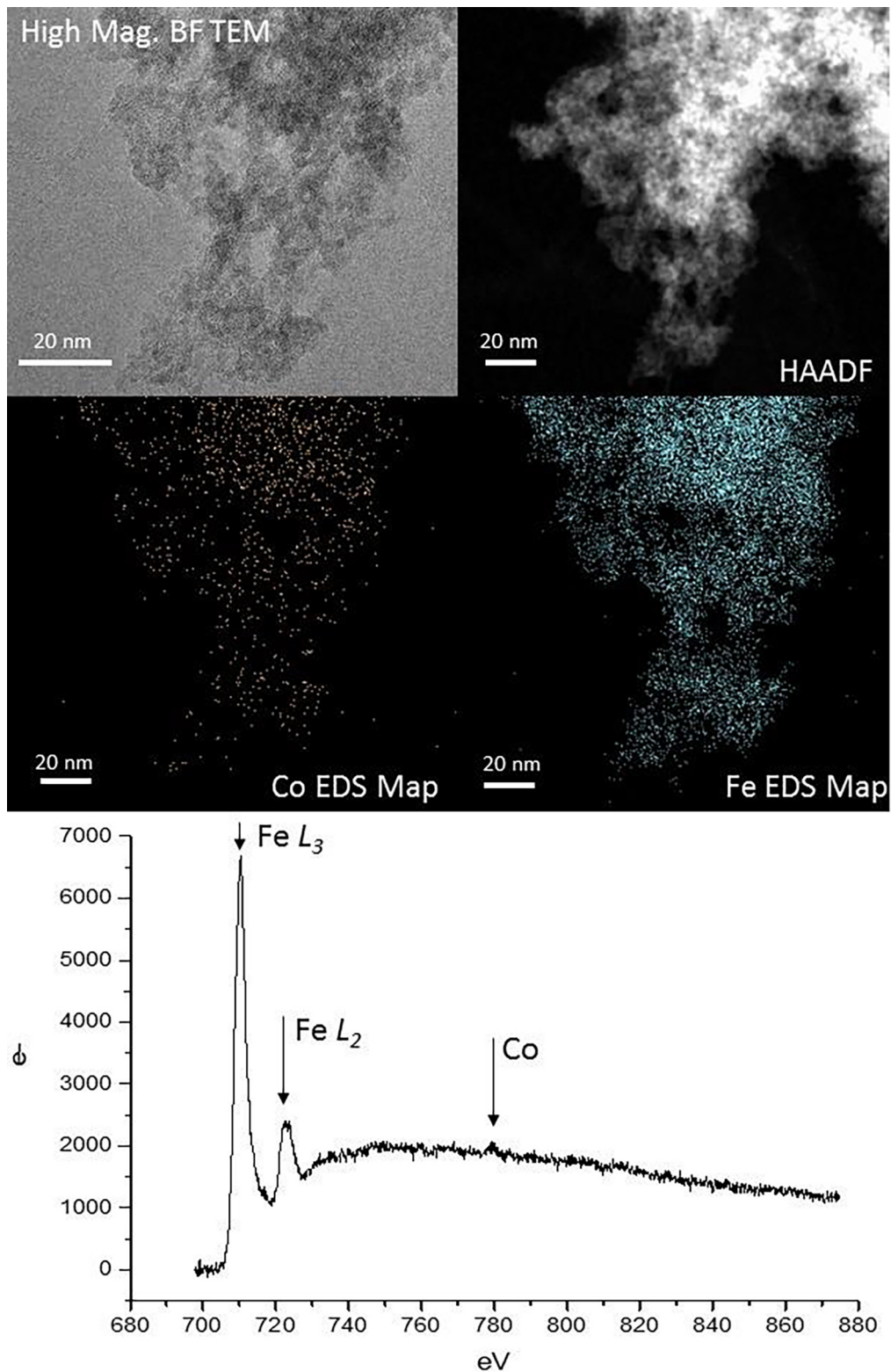
Fig. 6. High resolution bright field TEM image showing Fh particles after Co sorption at pH 8, with corresponding HAADF image and Co and Fe EDS maps of the same region. An electron energy loss spectrum collected from the Fh is also shown (bottom panel) with the position of the Fe $L_{3,2}$ and Co L_3-edges indicated.
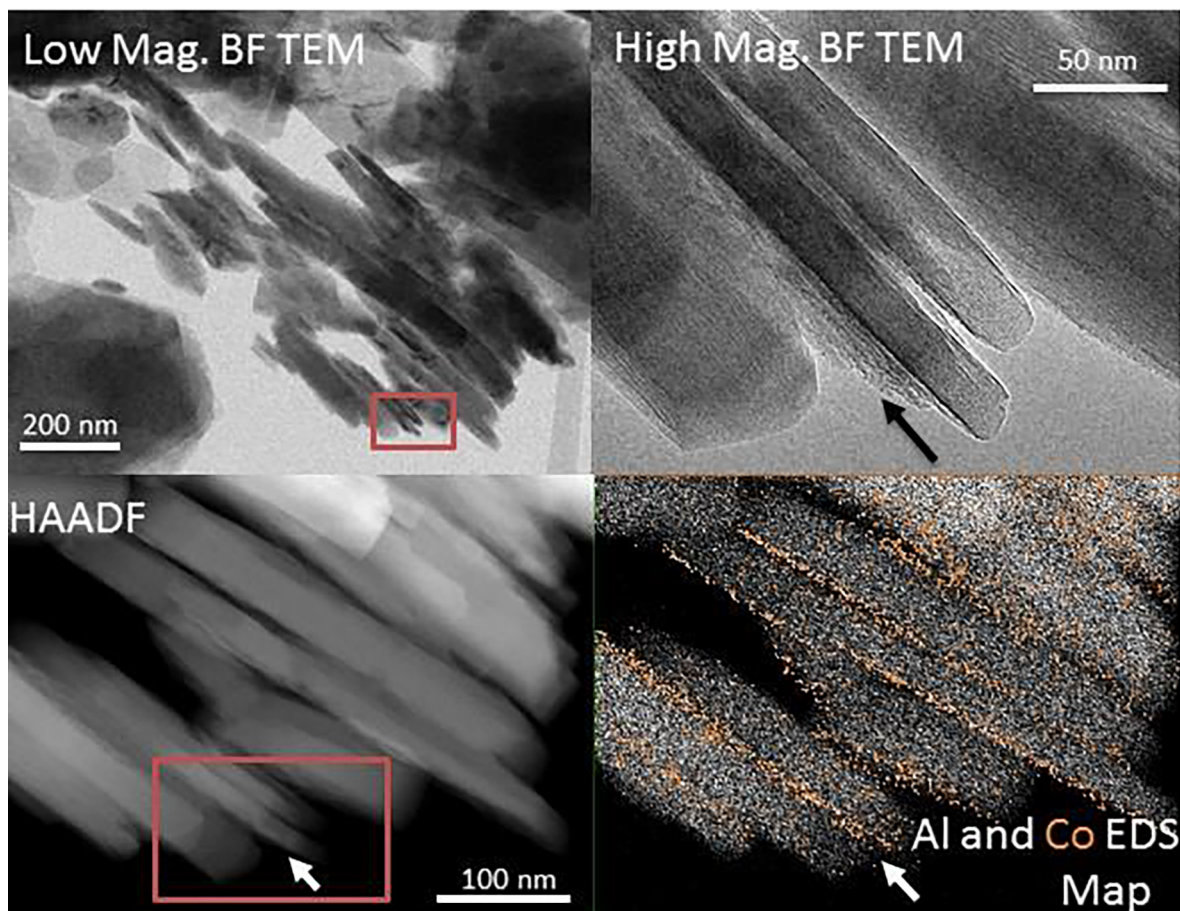
Fig. 7. Low resolution bright field TEM images show Ka crystals after Co sorption. Red box shows region chosen for high resolution TEM imaging. HAADF image of same region and Al and Co EDS elemental maps are also show. Arrows denote a specific Co-containing laminae and are the same location in each image. (For interpretation of the references to colour in this figure legend, the reader is referred to the web version of this article.)

Therefore we propose that Co binds to Fh via bi- or tri-nuclear surface complexes, and thus in summary via inner-sphere bidentate multinuclear edge-sharing complexes (Fig. 1C).

4.1.2. Co sorption to kaolinite

The sorption edge data for Ka (Fig. 2B) is similar to results found in previous studies (Spark et al., 1995; Angove et al., 1998; Landry et al., 2009). Our data sets all show increasing sorption between pH 4 and 5.5, and 6.5 and 8. In contrast to the Fh samples, the percentage of Co sorbed is somewhat dependent on initial Co concentration below pH ~ 7 (SI Fig. S1B), suggesting that our sorption systems are surface sorption site limited in the low-mid pH regime, consistent with the relatively low surface area for Ka (11.7 ± 0.1 m^2/g). Again in contrast to Fh, the Co sorption behaviour is also dependent on ionic strength mainly below pH ~ 7 (Fig. 2B), suggesting that Co binds to Ka via outer-sphere surface complexation in the low-mid pH regime. Taken together and in agreement with previous studies, these results suggest that Co binds to Ka via outer-sphere complexation during the initial sorption stage in the low-mid pH regime, where sorption is generally attributed to Co uptake onto permanently negatively

charged surface sorption sites present on the siloxane faces (Spark et al., 1995; Landry et al., 2009), and then above pH ~ 7 during the second sorption stage Co binds via inner-sphere complexation onto the variable charge sites present on the alumina faces that are increasingly deprotonated and thus negatively charged in the mid-high pH regime (Schulthess and Huang, 1990).

The above inferences about Co-Ka sorption behaviour based on our macroscopic sorption data are confirmed by our EXAFS analysis of Co sorbed to Ka, where at low-mid pH (pH 5 and 6) the best fits do not include Co-Al bonds, while at high pH (pH 8) the best fit includes 0.5 Al at ~ 2.9 Å. The number of Al backscatterers and the Co-Al interatomic distance indicates that octahedral Co-O moieties form inner-sphere bidentate edge-sharing complexes with AlOH octahedral surface groups at the pH value investigated (e.g., O'Day et al., 1994a,b). The absence and presence of Co-Al bonds at low-mid and high pH, respectively, also agrees with previous work on the sorption of Co to Ka (O'Day et al., 1994b). In addition to previous work however, our EDS map (Fig. 7) appears to show Co distributed across the edges of the Ka particles, and in particular concentrated onto one side of the edges of the Ka
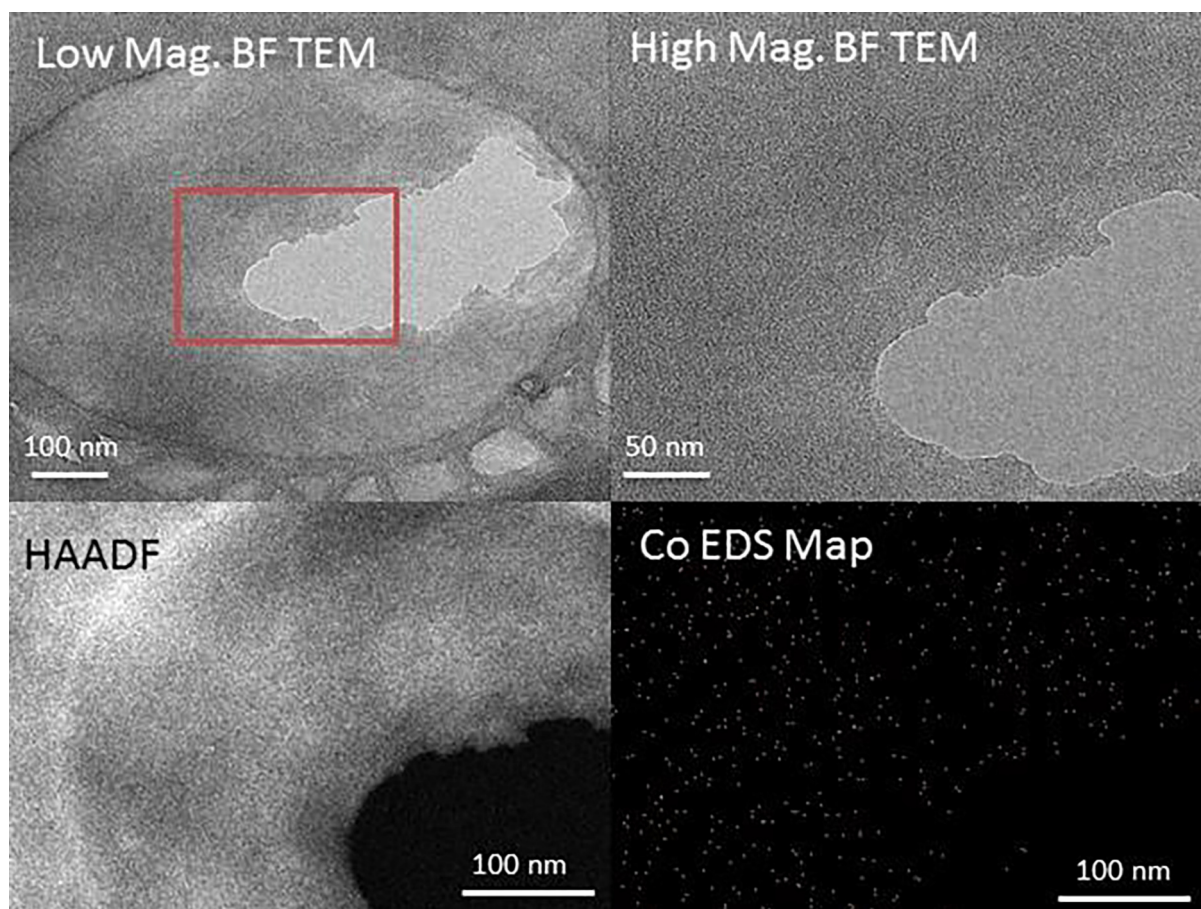
Fig. 8. Low resolution bright field TEM image showing HA after Co sorption at pH 8. Red box shows region show in the adjacent high resolution image with corresponding HAADF image of same region and the Co EDS elemental map. (For interpretation of the references to colour in this figure legend, the reader is referred to the web version of this article.)

particles. The distribution of Co across the particle edges is likely due to the presence of highly reactive edge sites created when crystallites break apart (Sposito, 1984) which Co can bind to (O'Day et al., 1994b). Additionally, Ka is a 1:1 clay that readily cleaves between octahedral Al and tetrahedral Si layers (Spark et al., 1995) to produce exposed AlOH and SiOH sites on opposite sides of the resultant crystallites. While the exposed SiOH sites are likely to provide outer-sphere sorption sites for Co, the exposed AlOH sites are known to provide inner-sphere sorption sites (O'Day et al., 1994b), and so we propose that the observed concentration of Co onto one side of the edges of the Ka particles is caused by a "depth profile" created when Co preferentially sorbs to cleavage planes containing exposed AlOH sites. As with Fh, the EXAFS analysis also indicates there are multiple ($\sim$1.5) Co-Co bonds at $\sim$3.1 Å, but the CN for the Co-Co pathway is not high enough to imply surface precipitation and there is no evidence of $Co(OH)_2$ nanoparticles present in the TEM images (Fig. 7). As with Fh, a Co-Co CN of $\sim$1.5 suggests a mixture of bi- and trinuclear surface complexes are forming. Overall we therefore propose that at low-mid pH, Co sorbs via outer-sphere complexation, likely associated with the permanently negatively charged sites present on the siloxane faces, while at high pH Co sorbs via inner-sphere bidentate binuclear edge-sharing complexes onto the variable charge alumina sites present at the Ka crystal edges and on exposed cleavage plains (Fig. 2).

4.1.3. Co sorption to humic acid

Our results show that there are significant differences in the apparent amount of Co sorbed to HA after filtration through 0.22 µm or 10 kDa filters (Fig. 3). The marked decrease in solid-associated Co above pH 5, which is only observed when using 0.22 µm filters, is attributed to HA solvation and dispersal processes occurring at higher pH values. HA solvation increases progressively as pH is raised from pH 2 to pH 12, with initially the low molecular weight (MW) fraction being dispersed at lower pH (cf. full dispersion of HA molecules is operationally defined at pH 12) (Ritchie and Posner, 1982). Therefore, at pH values > 5, a fraction of the sorbed Co present is not solid associated, but rather is bound to a relatively low MW (<220 nm) Co-HA phase that is dispersed in solution. The 10 kDa filter, in contrast, removed all HA particles larger than 3 nm (Pan et al., 2017) and represents the best estimate of true sorption behaviour (i.e. $\sim$90% above pH 6.5 for the 0.1 mol L^{-1} ionic strength system).

Co sorption to HA at low pH (pH 4 and 4.6) is reduced when the ionic strength is increased (Fig. 3), in

good agreement with previous studies on the sorption of other heavy metals onto purified Aldrich HA (Liu and Gonzalez, 2000), and our EXAFS analysis shows that at low pH (pH < 5) no Co-C bonds are required to fit the data (Table 1). This suggests that Co is bound through outer-sphere complexation at low pH. However, at higher pH Co sorption is unaffected by changes in ionic strength (Fig. 3) and our EXAFS fitting also includes 2 C at ~2.9 Å, indicative of inner-sphere complexation to C-containing functional groups present in HA. This is in good agreement with previous EXAFS studies reporting that Co is bound to HA via inner-sphere complexation to C atoms (Ghabbour et al., 2007; Xia et al., 1997). The presence of the Co-Co bond at 3.07 Å at pH 8 indicates the presence of a hydroxide-like precipitate, but again, the CN for the Co-Co pathway is not high enough to imply surface precipitation and the TEM images (Fig. 8) provide no evidence of Co-Co nanoclusters. This is consistent with other work on heavy metal interactions with organic matter, where Gustafsson et al. (2014) found that Cr(III) formed dimers when sorbed to soil above pH 5, with each Cr atom bound to two carboxyl groups at 2.85–2.87 Å, which is similar to the Co-C path length used in this study. Overall we propose that Co sorbs to HA at low pH via outer-sphere surface complexation, and at high pH via inner-sphere bidentate binuclear surface complexation, likely involving carboxyl groups present in the HA moiety.

4.2. Co sorption to organo-mineral composites

Sorption to all Fh-HA composites is enhanced relative to the pure Fh phase, particularly at low pH (Fig. 4A). This is typically attributed to the fact that, in contrast to Fh, the majority of HA surface functional groups are deprotonated at low pH and thus possess a negative charge, which when present in a Fh-HA composite results in enhanced sorption in the low-mid pH regime, over the pure end-member Fh phase (Tipping et al., 1983; Murphy and Zachara, 1995; Zhu et al., 2010). The combined sorption edge and EXAFS data for the Fh-HA system indicates that Co binds to each of the composite fractions at high pH (pH 8), and does so via the same molecular mechanisms as to the end-member Fh and HA phases. At pH 6 we see enhanced Co sorption relative to the end-member Fh (Fig. 4A), despite the EXAFS data only showing 6 Co-O pathways. The lack of a Co-Fe pathway is consistent with Co not sorbing to Fh below pH 6.5. The absence of a Co-C interatomic distance for the pH 6 Fh-HA sample is consistent with our EXAFS data for Co sorption to end-member HA which indicates that Co binds to HA via outer-sphere surface complexation at low-mid pH. In contrast at pH 7 the best fit EXAFS model includes 0.5 Fe at ~3.0 Å, 1.25 Co at ~3.17 Å and 1.1 C at ~2.87 Å, suggesting that Co binds to both the Fh fraction and the HA fraction, via the Fh inner-sphere multidentate binuclear surface complex and the HA inner-sphere bidentate binuclear surface complex. Our results indicate that the sorption behaviour of Co with respect to HA is the same for end-member HA, and HA that is sorbed to Fh surfaces.

Sorption to the Ka-HA composites is generally enhanced relative to the pure Ka phase, except for the 1.4 wt% C Ka-HA composite above pH ~ 7 (Fig. 4B), and again this is typically attributed to the presence of additional negatively charged sorption sites in the low-mid pH regime that are associated with the organic moieties (e.g., Heidmann et al., 2005a, who found that introducing fulvic acid to Ka increased Cu and Pb sorption at low to mid pH values). Consistent with the outer-sphere sorption of Co to end-member Ka and HA at low-mid pH, the best fit EXAFS models for Co sorption to Ka-HA at similar pH include only 6 O at ~2.0 Å. At higher pH (pH 8) the best fit EXAFS model includes 2 C at ~3.0 Å and 1 Co at ~3.14 Å (Table 2), suggesting that Co binds to the HA fraction via the inner-sphere bidentate binuclear surface complex identified for end-member HA. The pH 8 best fit EXAFS model does not however include any Co-Al bonds (Table 2), which suggests that either Co has a higher affinity for HA and is only sorbed to the HA phase in the composite, or because the Co-C and Co-Al bond lengths are similar they are not resolvable during the EXAFS analysis.

It is noteworthy that the extent to which Co sorption is enhanced in our mineral-organic composites over the pure end-member mineral phases appears to depend on the surface area of the end-member mineral phase. With relatively high surface area Fh ($\sim$295 ± 3 m^2/g) the percentage of Co sorbed by Fh-HA appears to be independent of composite C content, while with relatively low surface area Ka ($\sim$11.7 ± 0.1 m^2/g) the percentage of Co sorbed by Ka-HA appears to increase with increasing composite C content. This is observed in other heavy metal composite sorption systems, where studies using high surface area Fh in Fh-organic composites also show the enhanced low-mid pH regime sorption to be independent of composite C content (Moon and Peacock, 2012, 2013; Otero Fariña et al., 2018), while studies using relatively low surface area goethite ($\sim$42.1 m^2/g; Jönsson et al., 2006) in goethite-organic composites show increasingly enhanced low-mid pH regime sorption with increasing composite C content (Jönsson et al., 2006; Otero Fariña et al., 2017). We suggest that with a lower surface area, the organic surface coverage on a Ka composite will be significantly higher than for a Fh composite, and as such, cation sorption in the mid-low pH regime, where sorption onto the HA fraction dominates, will increasingly resemble the sorption of the cation onto pure end-member HA, and will thus increase with increasing HA fraction.

4.3. Surface complexation modeling of Co sorption to end-member ferrihydrite, kaolinite and humic acid

4.3.1. Model framework and input parameters

Surface complexation models were developed for the sorption of Co onto end-member Fh, Ka and HA that are consistent with the EXAFS data. The model framework for Co sorption to Fh is based on the model for copper sorption to Fh by Moon and Peacock (2013) and Otero Fariña et al. (2018), the framework for Co sorption to Ka is adapted from the model for Co sorption to Ka by Heidmann et al. (2005b), and the framework for Co sorption to HA is based on the model for copper sorption to HA by Otero Fariña et al. (2018). The model input

parameters were obtained either through fitting potentiometric titration data for the sorbent acid-base behaviour, or from direct measurement of the sorbent physiochemical characteristics, and are detailed in Moon and Peacock (2013) for Fh, Heidmann et al. (2005b) for Ka and López et al. (2012) for HA; the input parameters are reported here in Table 3.
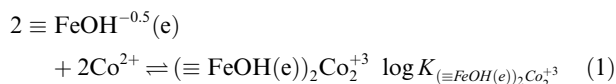
The BSM is used to model surface electrostatics in the Fh, Ka and HA sorption systems. For Fh, a 3-site 1 pK formalism is assumed for the protonation of the Fh surface, involving two types of singly-coordinated surface oxygens (sorbing cations in edge-sharing ($\equiv$FeOH$^{-0.5}$(e)) and corner-sharing ($\equiv$FeOH$^{-0.5}$(c)) configuration), and the triply coordinated oxygens ($\equiv$Fe$_3$O$^{-0.5}$) (e.g., Hiemstra et al., 1989; Hiemstra and van Riemsdijk, 2009; Moon and Peacock, 2013; Otero Fariña et al., 2018). A 2-site, 1pK formalism is used for the protonation of the Ka surface. This involves a singly-coordinated surface oxygen ($\equiv$AlOH$^{-0.5}$) representing the pH-dependent charge, and negatively charged sites ($\equiv$X$^-$) to represent the permanent negative charge (e.g., Heidmann et al., 2005b). For the HA, a 1-site 1 pK formalism is used, involving $\equiv$RCOO$^-$ sites where the stability constants for the protonation of these sites and the site densities are constrained using the NICA-Donnan model (Kinniburgh et al., 1999), calibrated on multiple data sets (López et al., 2012).

The sorption data are fit by iterating the log K for the surface complexation reaction that represents the formation of the Co-Fh, -Ka or -HA complexes that were identified by EXAFS analysis. The three Fh systems that contained 10^{-2} mol L^{-1} ionic strength (5.8, 0.58 and 0.058 wt% Co) and two of the Ka systems that contained 10^{-2} mol L^{-1} ionic strength (0.058 and 0.0058 wt% Co) are fit simultaneously. Due to the limitations of EQLFOR, systems with different ionic strengths are fit separately. The best fit log K values for the sorption of Co in all the end-member systems are

shown in Table 4. The model fits to the data are shown in Figs. 2 and 3.

4.3.2. Model for Co sorption to end-member ferrihydrite

Our EXAFS data indicate that Co sorbs to Fh via an inner-sphere bidentate bi- or tri-nuclear edge-sharing complex over the entire pH range investigated. Both bidentate bi- and tri-nuclear edge-sharing complexes were used to model the sorption edge data, however, models invoking a bidentate binuclear edge-sharing complex produce the best fits across all the Fh sorption data sets investigated. Model fits to the data are shown in Fig. 2 and our model produces adequate fits to the data over the range of ionic strengths studied. We therefore model our Fh sorption data with:

$$2 \equiv \mathrm{FeOH}^{-0.5}(e)$$
$$+ 2\mathrm{Co}^{2+} \rightleftharpoons (\equiv \mathrm{FeOH}(e))_2\mathrm{Co}_2^{+3} \quad \log K_{(\equiv FeOH(e))_2Co_2^{+3}} \quad (1)$$

$$K_{(\equiv FeOH(e))_2Co_2^{+3}}$$
$$= \frac{X_{(\equiv FeOH(e))_2Co_2^{+3}}\left(X_{\equiv FeOH^{-0.5}(e)}\right)^2 [Co^{2+}]}{} \exp\left(\frac{(-2\psi_0)F}{RT}\right) \quad (2)$$

where X represents the mole fraction of surface sites that the protonated or deprotonated surface complex occupies, ψ_0 is the electrostatic potential at the 0-plane (defined from the surface charge distribution (σ) using the BSM), F is the Faraday constant, R is the gas constant and T is temperature. It should be noted that bidentate binuclear edge-sharing complexation is technically represented by $\equiv$Fe(OH$^{-0.5}$(e))$_2$ + 2Co^{2+} $\rightleftharpoons$ $\equiv$Fe(OH(e))$_2$Co$_2^{3+}$. However, in surface complexation modeling formalism, $\equiv$FeOH$^{-0.5}$ is the operational surface site and thus both bidentate binuclear edge- and corner-sharing are represented by Eq. (1).

Table 3
Input parameters for the surface complexation models for Co sorbed to Fh, Ka and HA. Parameters for the $\equiv$FeOH$^{-0.5}$ site are from Moon and Peacock (2013); the $\equiv$AlOH$^{-0.5}$ and $\equiv$X$^-$ sites are from Heidmann et al. (2005b); and the $\equiv$RCOO$^-$ site are from López et al. (2012).

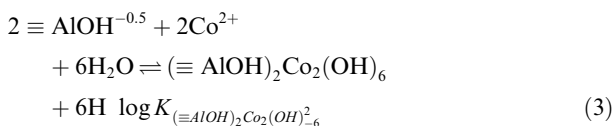| Site	Parameter	
$\equiv$FeOH$^{-0.5}$	Site density (mol sites g^{-1})	1.25×10^{-3}
	Capacitance (C) (F m^{-2})	1.1
	$LogK_{FeOH_2}$ $\equiv$FeOH$^{-0.5}$ + H$^+$ $\rightleftharpoons$ $\equiv$FeOH$_2^{+0.5}$	7.99
	$LogK_{FeOH_{Na}}$ $\equiv$FeOH$^{-0.5}$ + Na$^+$ $\rightleftharpoons$ $\equiv$FeOH$^{-0.5}$ $-$ Na$^{+0.5}$	-1.00
	$LogK_{FeOH_2{NO_3}}$ $\equiv$FeOH$_2^{+0.5}$ + NO$_3^-$ $\rightleftharpoons$ $\equiv$FeOH$_2^{+0.5}$ $-$ NO$_3^-$	-1.00
$\equiv$AlOH$^{-0.5}$	Site density (mol sites g^{-1})	8.78×10^{-4}
	Capacitance (C) (F m^{-2})	1.1
	$LogK_{AlOH_2}$ $\equiv$AlOH$^{-0.5}$ + H$^+$ $\rightleftharpoons$ $\equiv$AlOH$_2^{+0.5}$	4.8
	$LogK_{AlOH_{Na}}$ $\equiv$AlOH$^{-0.5}$ + Na$^+$ $\rightleftharpoons$ $\equiv$AlOH$^{-0.5}$ $-$ Na$^+$0.5	-2.1
	$LogK_{AlOH_2{NO_3}}$ $\equiv$AlOH$_2^{+0.5}$ + NO$_3^-$ $\rightleftharpoons$ $\equiv$AlOH$_2^{+0.5}$ $-$ NO$_3^-$	4.9
$\equiv$X$^-$	Site density (mol sites g^{-1})	5.44×10^{-5}
	Capacitance (C) (F m^{-2})	1.1
	$LogK_{X_{Na}}$ $\equiv$X$^-$ + Na$^+$ $\rightleftharpoons$ $\equiv$X$^-$ $-$ Na$^{+0.5}$	2.9
	$LogK_{X_H}$ $\equiv$X$^-$ + H$^+$ $\rightleftharpoons$ $\equiv$XH	5.9
$\equiv$RCOO$^-$	Site density (mol sites g^{-1})	1.94×10^{-3}
	Capacitance (C) (F m^{-2})	8.0
	$LogK_{RCOOH}$ $\equiv$RCOO$^-$ + H$^+$ $\rightleftharpoons$ $\equiv$RCOOH	3.60
	$LogK_{RCOO_{Na}}$ $\equiv$RCOO$^-$ + Na$^+$ $\rightleftharpoons$ $\equiv$RCOO$^-$ $-$ Na$^{+0.5}$	-1.00

Table 4
Log K values for Co sorbed to Fh, Ka and HA with the error ($\pm$) as derived from the sensitivity analysis.

Phase	Ionic strength (mol L^{-1})	Co concentration (wt% Co)	Complex	Log K
Fh	10^{-1}	0.58	$(\equiv FeOH(e))_2 2Co^{+3}$	13.11 ± 0.58
	10^{-2}	0.058, 0.58, 5.8	$(\equiv FeOH(e))_2 2Co^{+3}$	14.33 ± 2.07
	10^{-3}	0.58	$(\equiv FeOH(e))_2 2Co^{+3}$	13.90 ± 0.57
Ka	10^{-1}	0.058	$(\equiv AlOH^{-0.5})_2 Co_2(OH)_6^{-2}$	-33.86 ± 0.58
			X^--Co^{+2}	3.99 ± 0.49
	10^{-2}	0.58	$(\equiv AlOH^{-0.5})_2 Co_2(OH)_6^{-2}$	-33.97 ± 0.97
			$\equiv XH$	9.60 ± 1.17
		0.058	$(\equiv AlOH^{-0.5})_2 Co_2(OH)_6^{-2}$	-32.12 ± 0.8
			$XH-Co^{+2}$	9.23 ± 1.54
			X^--Co^{+2}	4.59 ± 3.02
		0.0058	$(\equiv AlOH^{-0.5})_2 Co_2(OH)_6^{-2}$	-31.46 ± 0.81
			$XH-Co^{+2}$	10.41 ± 1.62
			X^--Co^{+2}	5.20 ± 2.42
	10^{-3}	0.058	$(\equiv AlOH^{-0.5})_2 Co_2(OH)_6^{-2}$	-32.93 ± 1.58
			$XH-Co^{+2}$	11.72 ± 1.66
			X^--Co^{+2}	3.81 ± 5.85
HA	10^{-1}	0.58	$(\equiv RCOO)_2 Co_2$	-0.58 ± 2.25
			$\equiv RCOO^--Co^{+2}$	0.75 ± 0.94
	10^{-3}	0.58	$(\equiv RCOO)_2 Co_2$	2.04 ± 0.83
			$\equiv RCOO^--Co^{+2}$	2.03 ± 1.07

4.3.3. Model for Co sorption to end-member kaolinite

Our EXAFS data indicate that Co sorbs to Ka via an outer-sphere complex at low-mid pH and an inner-sphere bidentate binuclear edge-sharing complex associated with the alumina sorption sites at high pH. In agreement with previous modeling studies (e.g., Heidmann et al., 2005b; Peacock and Sherman, 2005) outer-sphere sorption is invoked onto the permanently negatively charged sites present on the siloxane faces ($\equiv X^-$), and we find that the best fits to the data generally involve Co sorption onto these sites in both their deprotonated ($\equiv X^-$) and protonated ($\equiv XH$) forms. The inner-sphere sorption is invoked onto the variable charge alumina sites ($\equiv AlOH^{-0.5}$). The total model fits to the data are shown in Fig. 2 while the contribution of the different surface sites to the total sorption is shown in Fig. 9. The protonated form of the permanently negatively charged site ($\equiv XH$) only significantly contributes to sorption at low ionic strength (Fig. 9A) and low wt% Co (SI Fig. S4A) and in the very low pH regime, reflecting the log K for the deprotonation of these sites (log K = 5.9; Table 3). Overall the models produce good fits to the data over the range of ionic strengths studied, and the contribution of the different surface complexes to the total sorption as a function of pH is consistent with our EXAFS data. We therefore model our Ka sorption data with:

$$2 \equiv AlOH^{-0.5} + 2Co^{2+}$$
$$+ 6H_2O \rightleftharpoons (\equiv AlOH)_2 Co_2(OH)_6$$
$$+ 6H \quad \log K_{(\equiv AlOH)_2 Co_2(OH)_6^{-2}} \tag{3}$$

$$K_{(\equiv AlOH)_2 Co_2(OH)_6^{-2}} = \frac{X_{(\equiv AlOH)_2 Co_2(OH)_6^{-2}}}{(X_{\equiv AlOH^{-0.5}})^2 [Co^{2+}]} \exp\left(\frac{(2\psi_0)F}{RT}\right) \tag{4}$$

$$\equiv X^- + Co^{2+} \rightleftharpoons \equiv X^- - Co^{2+} \quad \log K_{\equiv X^- - Co^{2+}} \tag{5}$$

$$K_{\equiv X^- - Co^{2+}} = \frac{X_{\equiv X^- - Co^{2+}}}{(X_{\equiv X^-})^2 [Co^{2+}]} \exp\left(\frac{(-2\psi_1)F}{RT}\right) \tag{6}$$

$$\equiv XH + Co^{2+} \rightleftharpoons \equiv XH - Co^{2+} \quad \log K_{\equiv XH - Co^{2+}} \tag{7}$$

$$K_{\equiv XH - Co^{2+}} = \frac{X_{\equiv XH - Co^{2+}}}{(X_{\equiv XH})^2 [Co^{2+}]} \exp\left(\frac{(-3\psi_1)F}{RT}\right) \tag{8}$$

where X represents the mole fraction of surface sites that the protonated or deprotonated surface complex occupies, ψ_0 is the electrostatic potential at the 0-plane and ψ_1 is the electrostatic potential at the 1-plane (as defined from the surface charge distribution (σ) using the BSM), F is the Faraday constant, R is the gas constant and T is temperature. Again it should be noted that bidentate binuclear edge-sharing complexation is technically represented by $\equiv Al(OH^{-0.5})_2 + 2Co^{2+} + 6H_2O \rightleftharpoons \equiv Al(OH)_2 Co_2(OH)_6 + 6H^+$. However, as above, in surface complexation modeling formalism $\equiv AlOH^{-0.5}$ is the operational surface site and thus both bidentate binuclear edge- and corner-sharing are represented by Eq. (3).

4.3.4. Model for Co sorption to end-member humic acid

Our EXAFS data indicate that Co sorbs to HA at low pH via outer-sphere surface complexation, and at high pH via inner-sphere bidentate binuclear surface complexation that likely involves carboxyl groups present in the HA moiety. It is not possible to determine from the EXAFS which sorption site(s) are most associated with the outer-sphere complex, and unlike Ka, HA has a number of different sorption sites which could be responsible for the electrostatic and hence outer-sphere sorption of Co (including carboxyl, phosphoryl, methoxyl, carbonyl, and alcoholic hydroxyl groups (Tsutsuki and Kuwatsuka, 1978; Yonebayashi and Hattori, 1988)). Given this we nominally assign the outer-sphere sorption to the carboxyl
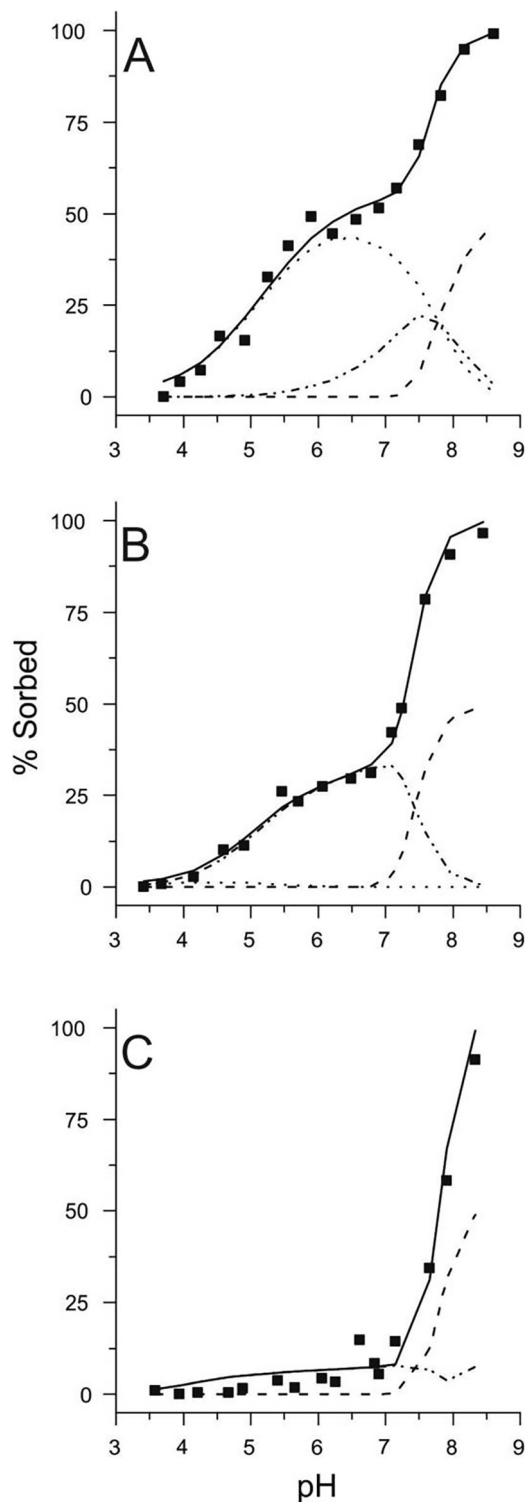
Fig. 9. Iterated surface complexation model predictions for Co sorption to Ka surface sites. Panel A shows Co sorption with an ionic strength of 10^{-3} mol L^{-1}; panel B, 10^{-2} mol L^{-1}; and panel C, 10^{-1} mol L^{-1}. Squares are data; solid lines show total predicted sorption; dashed lines, $\equiv$AlOH sites; dotted lines, $\equiv$XH sites; and dash-dot-dot lines, $\equiv$X^{-} sites.
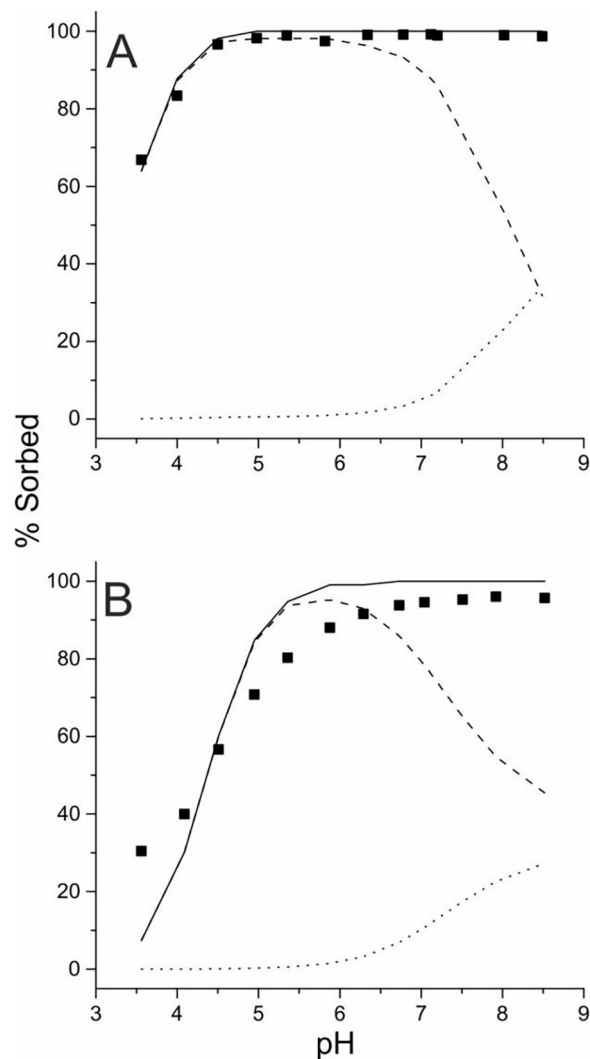

Fig. 10. Iterated surface complexation model predictions for Co onto HA surface sites at 10^{-3} mol L^{-1} NaNO$_3$ (panel A) and 10^{-1} mol L^{-1} NaNO$_3$ (panel B). Squares are data; solid lines, total predicted sorption; dashes, outer-sphere sorption to $\equiv$RCOO^{-} sites; and dots, inner-sphere sorption to $\equiv$RCOO^{-} sites.

$\equiv$RCOO^{-} sites in the modeling, which is at least consistent with the fact that Co is already known to interact with these sites during sorption to HA via inner-sphere complexation (as identified for our high pH Co-HA sorption sample and by Xia et al. (1997) and by Ghabbour et al. (2007) during their studies of Co sorption to HA). The total model fits to the data are shown in Fig. 3 while the contribution of the different surface sites to the total sorption is shown in Fig. 10. Overall the models produce adequate fits to the data at the two ionic strengths studied, and the contribution of the different surface complexes to the total sorption as a function of pH is consistent with our EXAFS data. We therefore model our HA sorption data with:
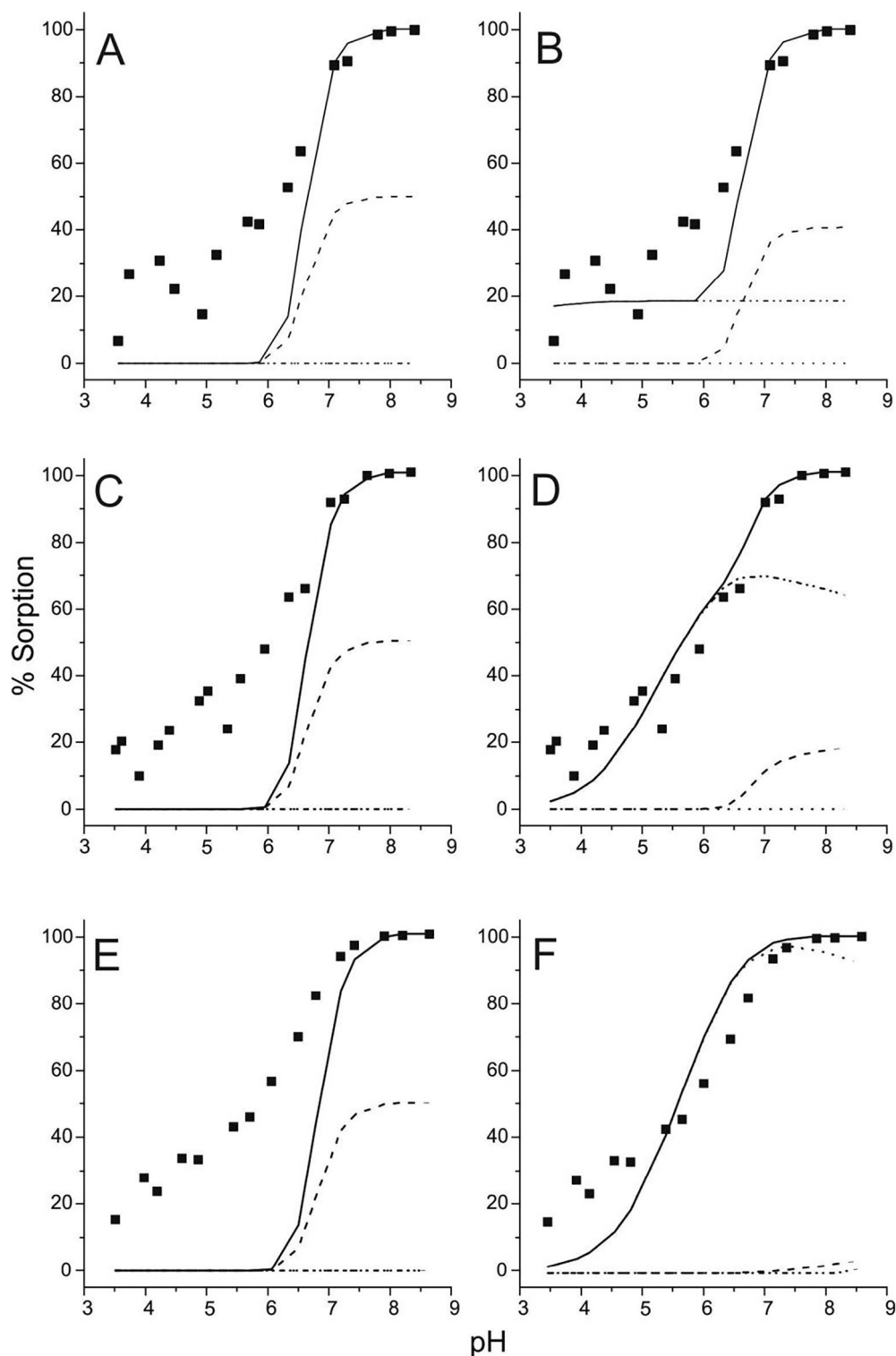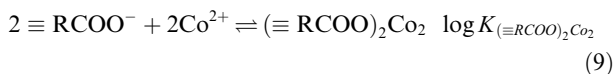
Fig. 11. Surface complxeation model predictions of Co sorption to Fh-HA surface sites. Panels A and B show the composite with 5 wt% C; panels C and D, 10 wt% C; and panels E and F, 17 wt% C composite. Panels A, C, and E show predicted sorption using log K's fixed to those from the two end–member phases. Panels B, D, and F show predicted sorption with iterated log K's. Solid lines show total predicted sorption; dashed lines, sorption to ≡FeOH sites; dash-dot-dot, outer-sphere sorption to ≡RCOO⁻ sites; and dotted lines, inner-sphere sorption to ≡RCOO⁻ sites.

$$2 \equiv RCOO^- + 2Co^{2+} \rightleftharpoons (\equiv RCOO)_2Co_2 \quad \log K_{(\equiv RCOO)_2Co_2} \tag{9}$$

$$K_{(\equiv RCOO)_2Co_2} = \frac{X_{(\equiv RCOO)_2Co_2}}{(X_{\equiv RCOO^-})^2[Co^{2+}]} \exp\left(\frac{(-4\psi_0)F}{RT}\right) \tag{10}$$

$$\equiv RCOO^- + Co^{2+} \rightleftharpoons \equiv RCOO^-$$
$$- Co^{2+} \quad \log K_{\equiv CROO^- - Co^{2+}} \tag{11}$$

$$K_{\equiv RCOO^- - Co^{2+}} = \frac{X_{\equiv RCOO^- - Co^{2+}}}{(X_{\equiv RCOO^-})^2[Co^{2+}]} \exp\left(\frac{(-2\psi_1)F}{RT}\right) \tag{12}$$

As for the Fh and Ka equations, X represents the the mole fraction of surface sites that the protonated or deprotonated surface complex occupies, ψ_0 is the electrostatic potential at the 0-plane and ψ_1 is the electrostatic potential at the 1-plane (as defined from the surface charge distribution (σ) using the BSM), F is the Faraday constant, R is the gas constant and T is temperature.

4.3.5. Sensitivity analysis

A sensitivity analysis of the systems, to test the models' sensitivity to the input parameters, was conducted, in which the input parameters are varied over a range of reasonable experimental and theoretical values. The process for this is
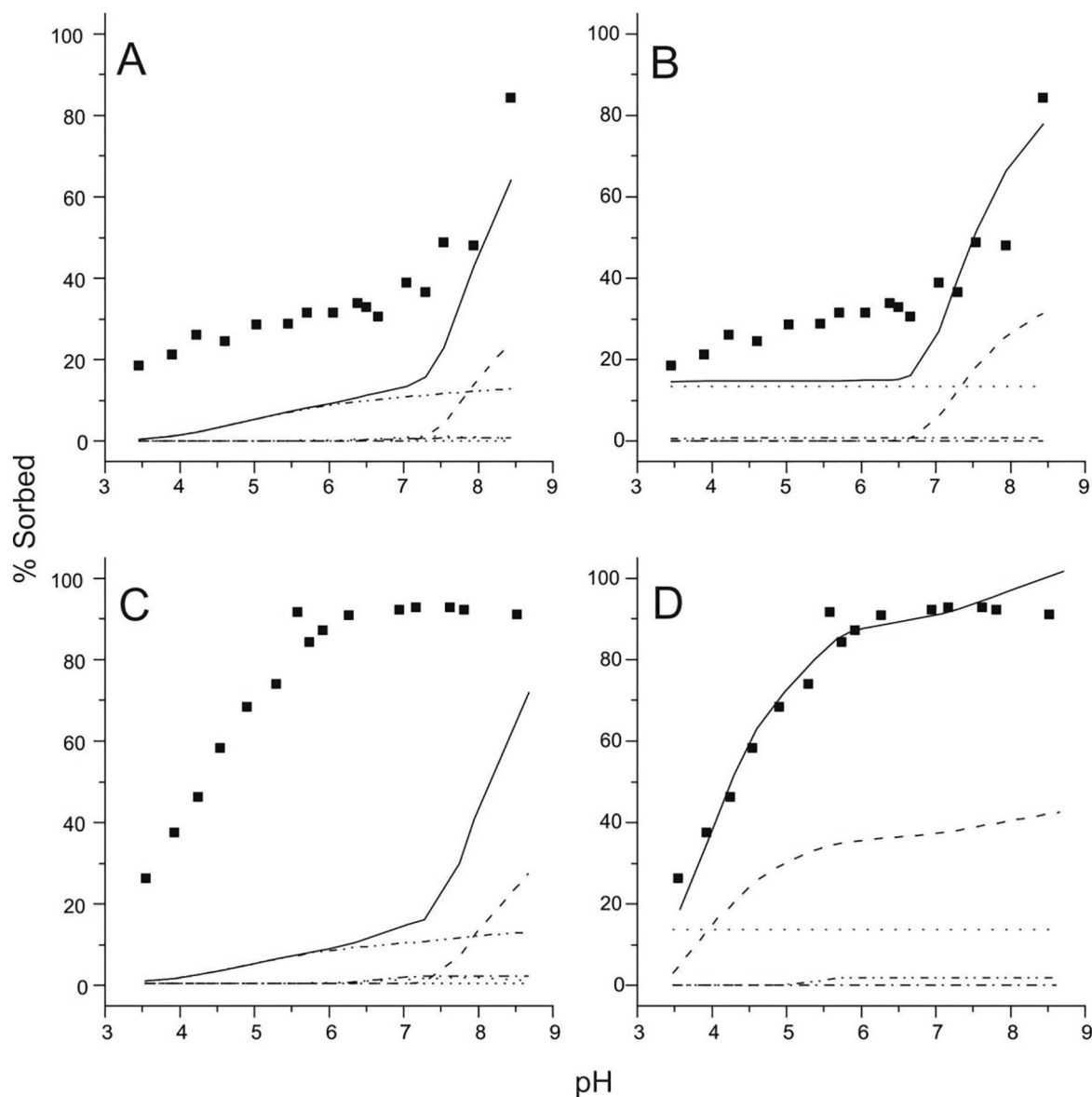

Fig. 12. Surface complxeation model predictions of Co sorption to Ka-HA surface sites. Panels A and B show the results for the 1.4 wt% C composite, and panels C and D show the 2.2 wt% C composite. Panels A and C show predicted sorption using log K's fixed to those from the two end-member phases. Panels B and D show predicted sorption with iterated log K's. Solid lines show total predicted sorption; dashed lines, sorption to the $\equiv$AlOH sites; dotted lines, sorption to $\equiv$XH sites; dash-dot-dot lines, inner-sphere sorption to $\equiv$RCOO$^-$ sites; and dash-dot, outer-sphere sorption to $\equiv$RCOO$^-$ sites.

described fully in the SI, and the results of the analysis are shown in Table 4 as the error ($\pm$). The errors provide an estimate of the range that the log K values may vary due to inherent uncertainties in the parameterisation of the Fh, Ka, and HA sorption properties in the models. Overall, based on our EXAFS identified surface complexes, the average log K for Co sorption onto Fh is log K ($\equiv$FeOH(e))$_2$Co$_2^{+3}$ = 13.78; onto Ka is log K $\equiv$X$^-$–Co^{+2} = 4.4, log K $\equiv$XH–Co^{+2} = 10.24 and log K ($\equiv$AlOH)$_2$Co$_2$(OH)$_6$ = -32.868; and onto HA is log K $\equiv$RCOO$^-$–Co^{+2} = 1.39 and log K ($\equiv$RCOO)$_2$Co$_2$ = 0.73.

4.4. Surface complexation modeling of Co sorption to organo-mineral composites

4.4.1. Model framework and input parameters

Sorption edge data for the Fh-HA and Ka-HA composites is intermediate between the end member phases (Fig. 4), and the EXAFS data shows the Co sorption to the composites occurs via the same molecular mechanisms as to the end-member phases (Tables 1 and 2, Fig. 5). This suggests that Co sorption to these composites shows a degree of additivity, and therefore a component additivity approach was used to fit the Fh-HA and Ka-HA composite sorption data. In this approach the models for Co sorbed to Fh and HA, and Ka and HA are combined linearly in order to create a single sorption model for each composite. The model input parameters are reported here in Table 3 and the model fits are shown in Fig. 11 (panels A, C, and E) and Fig. 12 (panels A and C). As with the end-member models, the BSM is used to model the composite electrostatics. As the linear combination of the Fh and HA end-member models, the Fh composite adopted a 4-site 1 pK formalism (containing the 3 Fh sites and the 1 HA site) while the Ka composite adopted a 3 pK formalism (the 2 Ka sites and the 1 HA site). In this approach the log K's for the protonation and binding of electrolyte ions to these sites, and absolute site densities, are fixed to the values of the end-member Fh or Ka and HA models. Operational site densities for each site, and a surface area and Stern layer capacitance for each composite, are then calculated from the end-member values weighted to the appropriate Fh:HA or Ka:HA mass ratio (Table 5). Initially Co sorption to the composites is modelled with the best fit log K values from the end-member systems (Figs. 11A, C, E and 12A, C).

The end-member log K values are then iterated whilst keeping all other parameters constant (Figs. 11B, D, F and 12B, D). If the composites behave in an additive manner then the optimised log K values should fall within the uncertainties on the end-member values.

4.4.2. Model for Co sorption to Fh-HA composite

Model fits for Co sorption to the 3 Fh-HA composites are shown in Fig. 11. Using the exact end-member log K's, the model underestimates Co sorption to the 5, 10, and 17 wt% C Fh-HA composites below pH 6.5 (Fig. 11). When the log K values are iterated (Table 6) the fit improves, but for the 5 wt% C composite there is still a significant underestimation between pH 5 and 6.5 (Fig. 11B). Furthermore, the log K for the outer-sphere HA complex in the iterated fits for all composites is far outside the uncertainty on the end-member value (Table 4). This implies that the model formalism for the outer-sphere complexation of Co to the end-member HA does not accurately describe

Table 6
Iterated log K values for Co sorbed to Fh and Ka and HA organo-mineral composites.

System	Complex	Log K
Fh-HA 5 wt% C	($\equiv$FeOH(e))$_2$2Co^{+3}	13.11
	($\equiv$RCOO)$_2$Co$_2$	-0.58
	$\equiv$RCOO$^-$—Co^{+2}	10.73
Fh-HA 10 wt% C	($\equiv$FeOH(e))$_2$2Co^{+3}	13.11
	($\equiv$RCOO)$_2$Co$_2$	-0.58
	$\equiv$RCOO$^-$—Co^{+2}	9.23
Fh-HA 17 wt% C	($\equiv$FeOH(e))$_2$2Co^{+3}	13.11
	($\equiv$RCOO)$_2$Co$_2$	-0.58
	$\equiv$RCOO$^-$—Co^{+2}	8.86
Ka-HA 1.4 wt% C	2AlOH-2Co	-30.67
	XH—Co^{+2}	18.31
	X$^-$—Co^{+2}	4.22
	($\equiv$RCOO)$_2$Co$_2$	15.35
	$\equiv$RCOO$^-$—Co^{+2}	2.10
Ka-HA 2.2 wt% C	2AlOH-2Co	-16.82
	XH—Co^{+2}	26.49
	X$^-$—Co^{+2}	5.17
	($\equiv$RCOO)$_2$Co$_2$	2.83
	$\equiv$RCOO$^-$—Co^{+2}	2.03

Table 5
Input parameters for the surface complexation models for Co sorbed to Fh and Ka organo-mineral composites. Operational site densities for each site, and a surface area and Stern layer capacitance for each composite, are then calculated from the end-member values weighted to the appropriate Fh:HA or Ka:HA mass ratio. Fh data is from Moon and Peacock (2013), Ka from Heidmann et al. (2005b), and HA from López et al. (2012).

Composite		Site densities (mol sites L^{-1})				Surface area (m^2 L^{-1})	Stern layer capacitance (F m^{-2})
		FeOHe	FeOHc	Fe3O	HA-COO$^-$		
FhHA	5 wt% C	1.13×10^{-3}	1.58×10^{-3}	5.4×10^{-4}	1.93×10^{-5}	291.62	1.8
	10 wt% C	9.96×10^{-3}	1.39×10^{-3}	4.79×10^{-4}	3.85×10^{-5}	281.23	2.5
	17 wt% C	8.35×10^{-4}	1.17×10^{-3}	4.02×10^{-4}	6.27×10^{-5}	268.14	3.39
		X$^-$	AlOH	HA-COO$^-$			
KaHA	1.4 wt% C	1.33×10^{-5}	2.14×10^{-3}	1.45×10^{-6}		16.86	1.83
	2.2 wt% C	1.3×10^{-5}	2.1×10^{-3}	2.28×10^{-6}		19.81	1.4

the outer-sphere complexation of Co to the HA fraction of the composite. This could be because the functional groups available for outer-sphere complexation in the composite are modified as a result of HA interaction with the Fh surface. The model also fails to accurately predict the distribution of the adsorbed Co between the Fh and HA fractions, where, based on our EXAFS, the model fits should show inner-sphere bidentate binuclear sorption to the Fh fraction, either no sorption or outer-sphere sorption to the HA fraction at mid-low pH and inner-sphere bidentate binuclear sorption to both the Fh and HA fractions at mid-high pH. As such Co sorption to our Fh organo-mineral composites is non-additive and cannot be modelled assuming a component additivity approach. This is in contrast to previous work on Cu sorption to Fh-HA composites, where iterated log K values (resulting in log K values of 9.27 and 3.31 for Cu sorption to Fh and HA, respectively) remained within the range of error determined by a sensitivity analysis and produced a good fit to the data, showing that a component additivity approach was able to accurately predict the sorption behaviour (Otero-Fariña et al., 2018).

4.4.3. Model for Co sorption to Ka-HA composite

The model fits for Co sorption to the 2 KaHA composites are shown in Fig. 12. Using the exact end-member log K's, the model underestimates Co sorption to the 1.4 and 2.2 wt% C KaHA composite over the entire pH range (Fig. 12). When the log K values are iterated (Table 6) the fit improves, but there is still an underestimation between pH 4 and 7 for the 1.4 wt% C composite. Furthermore, for the 1.4 wt% C composite the log K values for the $\equiv$XH–Co^{+2} and inner-sphere HA complex are outside the uncertainty on the end-member values (Table 4), and for the 2.2 wt% C composite the log K values for the $\equiv$XH–Co^{+2} and inner-sphere Ka complex are outside the uncertainty on the end-member values (Table 4). As for the Fh-HA composite, this suggests that these surface functional groups behave differently in the composite system compared to the single phase systems. This could be caused by fractionation of HA during adsorption to Fh or Ka in the preparation of the composites. High and low molecular weight HA could become fractionated in this process and so the HA associated with the minerals is not the same as the HA involved in the sorption of Co to HA end-member system. For both composites the model also fails to accurately predict the distribution of the adsorbed Co between the Ka and HA fractions, where, based on our EXAFS, the model fits should show outer-sphere sorption to either the Ka or HA fractions at mid-low pH and inner-sphere bidentate binuclear sorption to the HA fraction and either no sorption or inner-sphere bidentate binuclear sorption to the Ka fraction at mid-high pH. As such Co sorption to our Ka organo-mineral composites is non-additive and cannot be modelled assuming a component additivity approach.

4.5. Implications for Co behaviour in natural environments

In all end-member and organo-mineral composite systems studied in this work, inner-sphere bidentate binuclear sorption complexes were found to occur at mid-high pH.

We propose that this is a universal uptake mechanism for Co in soils and sediments at neutral and alkaline pH values. This universal sorption mechanism controls Co uptake onto Fh, Ka and HA and their associated organo-mineral composites, and limits Co mobility in natural and contaminated environments. Our work unifies previous studies that have worked on similar systems individually yet reported similar sorption mechanisms (O'Day et al., 1994a,b; Xia et al., 1997; Ghabbour et al., 2007), but also reconciles direct observations of Co sorption mechanisms, observed with EXAFS, with indirect Co sorption modeling studies, by developing the first thermodynamic surface complexation models for Co sorption to Fh, Ka and HA that are completely consistent with EXAFS results.

Our results indicate that Co sorption behaviour is likely to differ between environments where the organic matter content varies. In soils that are low in organic matter such as some alluvial sediments and desert areas, Co will behave similarly to how it does in the pure mineral systems as there is no organic matter to influence sorption. This means that Co will be mobile below pH $\sim$ 6.5 because below this pH there is no significant sorption to solid phases likely to be present such as iron (hydr)oxides and clay minerals. In contrast to mineral soils, in peat soils and other organic matter dominated environments, Co will be less mobile at lower pH values due to higher sorption to humic substances and will likely be mobile as Co^{2+} only at very low pH values. At neutral to high pH, HA may also be present as colloids and the association of Co with low MW HA colloids is a potential transport vector for contamination in organic rich environments at neutral to alkaline pH values where high Co sorption would be expected. In temperate regions, soils that contain both minerals and modest amounts of organic matter are much more common than either mineral or peat soils and are likely to show sorption behaviour that is composite between pure mineral and organic dominated systems. This is especially true at low pH, where enhanced sorption may be expected due to interaction of Co with humic materials. Also, in composite systems discrete HA colloids do not appear to form, most likely due to the strong bonding of HA to mineral surfaces reducing the propensity for HA solvation and dispersion in solution. In addition, in soils where there is a high amount of humic substances relative to clays, sorption to the clay fraction may be completely inhibited due to all AlOH sites being involved in clay-HA bonding and none being available for cation sorption. This would result in Co binding solely to the HA coating and thus sorption behaviour would be most similar to that of the pure HA system.

Finally these organo-mineral composite systems cannot be modelled in a component additivity approach. Therefore, the physiochemical characteristics of the composite must be so significantly different from the end-member phases that adsorption is not the simple linear combination of the end-member adsorptivities. This means that Co sorption to these composites cannot currently be predicted and more research is necessary in order to fully understand how organic and mineral phases in organo-mineral composites interact to potentially change the composite adsorptive properties.

5. CONCLUSION

The addition of HA to Fh and Ka enhances the amount of Co sorbed below pH 6, where there is typically little sorption. For the first time, Co sorption onto an iron (oxy)hydroxide was studied using EXAFS and its local molecular environment analysed. EXAFS and TEM data suggests that Co sorbs to all soil components through formation of similar inner-sphere bidentate multinuclear surface complexes at high pH, but at low pH Co sorption to Ka and HA is via outer-sphere complexation. We conclude that the formation of these inner-sphere bidentate multinuclear surface complexes at high pH constitute a universal uptake mechanism of Co onto soil materials. It was possible to fit the sorption data for the pure end-member systems invoking the sorption mechanisms identified by the EXAFS data. However, fixing the log K's in the composite models to the values from the pure end-member systems did not produce a good fit to the composite sorption data. Therefore, we conclude that Co sorption to Fh-HA and Ka-HA composites is non-additive and further work is required to understand how organic and mineral phases in organomineral composites interact and how this interaction potentially changes composite adsorptive properties.

REFERENCES

Ainsworth C. C., Pilon J. L., Gassman P. L., Van W. G. and Sluys D. (1994) Cobalt, cadmium, and lead sorption to hydrous iron oxide: residence time effect. *Soil Sci. Soc. Am. J.* **58**, 1615–1623.

Alvarez A. and Garrido J. (2004) Retention of Co (II), Ni (II), and Cu (II) on a purified brown humic acid. Modeling and characterization of the sorption process. *Langmuir* **20**, 3657–3664.

Angove M. J., Johnson B. B. and Wells J. D. (1997) Adsorption of cadmium(II) on kaolinite. *Colloids Surf., A* **126**(2–3), 137–147. https://doi.org/10.1016/S0927-7757(96)03990-8.

Angove M. J., Johnson B. B. and Wells J. D. (1998) The influence of temperature on the adsorption of cadmium(II) and cobalt(II) on kaolinite. *J. Colloid Interf. Sci.* **204**, 93–103.

Charlton S. R. and Parkhurst D. L. (2002) PHREEQCI – A Graphical User Interface to the Geochemical Model PHREEQC. U.S. Geological Survey Fact Sheet FS-031–02.

Davis A. P. and Bhatnagar V. (1995) Adsorption of cadmium andhumic acid onto hematite. *Chemosphere* **30**, 243–256.

Eick M. J. and Fendorf S. E. (1998) Reaction sequence of nickel(II) with kaolinite: mineral dissolution and surface complexation and precipitation. *Soil Sci. Soc. Am. J.* **62**, 1257–1267.

Forbes E. A., Posner A. M. and Quirk J. P. (1976) The specific adsorption of divalent Cd Co, Cu, Pb, and Zn on goethite. *J. Soil Sci.* **27**, 154–166.

Fortin D. and Langley S. (2005) Formation and occurrence of biogenic iron-rich minerals. *Earth-Sci. Rev.* **72**, 1–19.

Gál J., Hursthouse A., Tatner P., Stewart F. and Welton R. (2008) Cobalt and secondary poisoning in the terrestrial food chain: data review and research gaps to support risk assessment. *Environ. Int.* **34**(6), 821–838. https://doi.org/10.1016/j.envint.2007.10.006.

Ghabbour E. A., Scheinost A. C. and Davies G. (2007) XAFS studies of cobalt(II) binding by solid peat and soil-derived humic acids and plant-derived humic acid-like substances. *Chemosphere* **67**(2), 285–291. https://doi.org/10.1016/j.chemosphere.2006.09.094.

Gustafsson J. P., Persson I., Oromieh A. G., Van Schaik J. W. J., Sjö C. and Kleja D. B. (2014) Chromium(III) complexation to natural organic matter: mechanisms and modeling. *Environ. Sci. Technol.* **48**, 1753–1761. https://doi.org/10.1021/es404557e.

Heidmann I., Christl I. and Kretzschmar R. (2005a) Sorption of Cu and Pb to kaolinite-fulvic acid colloids: assessment of sorbent interactions. *Geochim. Cosmochim. Ac.* **69**(7), 1675–1686. https://doi.org/10.1016/j.gca.2004.10.002.

Heidmann I., Christl I., Leu C. and Kretzschmar R. (2005b) Competitive sorption of protons and metal cations onto kaolinite: experiments and modeling. *J. Colloid Interf. Sci.* **282**, 270–282. https://doi.org/10.1016/j.jcis.2004.08.019.

Hiemstra T., De Wit J. C. M. and Van Riemsdijk W. H. (1989) Multisite Proton Adsorption Modeling at the Solid/Solution Interface of(Hydr)oxides: A New Approach II. Application to Various Important (Hydr)oxides. *J. Colloid Interf. Sci.*

Hiemstra T. and Van Riemsdijk W. H. (2009) A surface structural model for ferrihydrite I: Sites related toprimary charge, molar mass, and mass density. *Geochim. Cosmochim. Acta.*

Hewitt E. J. (1953) Metal interrelationships in plant nutrition. *J. Exp. Bot.* **4**(1), 59–64. https://doi.org/10.1093/jxb/4.1.59.

Iglesias A., López R., Gondar D., Antelo J., Fiol S. and Arce F. (2010) Adsorption of paraquat on goethite and humic acid-coated goethite. *J. Hazard. Mater.* **183**, 664–668.

Jönsson J., Sjöberg S. and Lövgren L. (2006) Adsorption of Cu(II) to schwertmannite and goethite in presence of dissolved organic matter. *Water Res.* **40**(5), 969–974. https://doi.org/10.1016/j.watres.2006.01.006.

Kanungo S. B. (1994) Adsorption of cations on hydrous oxides of iron. *J. Colloid Interf. Sci.* **162**, 93–102.

Kinniburgh D. G., Van Riemsdijk W. H., Koopal L. K., Borkovec M., Benedetti M. F. and Avena M. J. (1999) Ionbinding to natural organic matter: competition, heterogeneity, stoichiometry and thermodynamic consistency. *Colloid. Surface. A Physicochem. Eng. Asp.* **151**, 147–166.

Landry C. J., Koretsky C. M., Lund T. J., Schaller M. and Das S. (2009) Surface complexation modeling of Co(II) adsorption on mixtures of hydrous ferric oxide, quartz and kaolinite. *Geochim. Cosmochim. Acta* **73**, 3723–3737. https://doi.org/10.1016/j.gca.2009.03.028.

Liu A. and Gonzalez R. D. (2000) Modeling adsorption of copper (II), cadmium(II) and lead (II) on purified humic acid. *Adsorpt. J. Int. Adsorpt. Soc.* **16**, 3902–3909.

López R., Gondar D., Antelo J., Fiol S. and Arce F. (2011) Proton binding on untreated peat and acid-washed peat. *Geoderma* **164**, 249–253.

López R., Gondar D., Antelo J., Fiol S. and Arce F. (2012) Study of the acid-base properties of a peat soil and its humin and humic acid fractions. *Eur. J. Soil Sci.* **63**(4), 487–494. https://doi.org/10.1111/j.1365-2389.2012.01461.x.

McLaren R. G., Lawson D. M. and Swift R. S. (1986) Sorption and desorption of cobalt by soils and soil components. *J. Soil Sci.* **37**(3), 413–426.

Moon E. M. and Peacock C. L. (2012) Adsorption of Cu(II) to ferrihydrite and ferrihydrite-bacteria composites: importance of the carboxyl group for Cu mobility in natural environments. *Geochim. Cosmochim. Acta* **92**, 203–219. https://doi.org/10.1016/j.gca.2012.06.012.

Moon E. M. and Peacock C. L. (2013) Modelling Cu(II) adsorption to ferrihydrite and ferrihydrite-bacteria composites: deviation from additive adsorption in the composite sorption system. *Geochim. Cosmochim. Acta* **104**, 148–164. https://doi.org/10.1016/j.gca.2012.11.030.

Murphy E. M. and Zachara J. M. (1995) The role of sorbed humic substances on the distribution of organic and inorganic contaminants in groundwater. *Geoderma* **67**, 103–124.

O'Day P. A., Brown, Jr., G. E. and Parks G. A. (1994a) X-ray absorption spectroscopy of cobalt(II) multinuclear surface complexes and surface precipitates on kaolinite. *J. Colloid Interf. Sci.* **165**, 269–289.

O'Day P. A., Parks G. A. and Brown, Jr, G. E. (1994b) Molecular structure and binding sites of cobalt(II) surface complexes on kaolinte from X-ray absorption spectroscopy. *Clays Clay Miner.* **42**(3), 337–355.

Otero-Fariña A., Fiol S., Arce F. and Antelo J. (2017) Effects of natural organic matter on the binding of arsenate and copper onto goethite. <https://doi.org/10.1016/j.chemgeo.2017.04.012>.

Otero-Fariña A., Peacock C. L., Fiol S., Antelo J. and Carvin B. (2018) A universal adsorption behaviour for Cu uptake by iron (hydr)oxide organo-mineral composites. *Chem. Geol.*. https://doi.org/10.1016/j.chemgeo.2017.12.022.

Pan C., Troyer L. D., Liao P., Catalano J. G., Li W. and Giammar D. E. (2017) Effect of humic acid on the removal of chromium (VI) and the production of solids in iron electrocoagulation. *Environ. Sci. Technol* **51**. https://doi.org/10.1021/acs.est.7b00371.

Parkhurst D. L. and Appelo C. A. J. (1999) User's Guide to PHREEQC (version 2) – a computer program for speciation, batch-reaction, one-dimensional transport, and inverse geochemical calculations. U.S. Geological Survey Water-Resources Investigations Report 99–4259.

Peacock C. L. and Sherman D. M. (2005) Surface complexation model for multisite adsorption of copper(II) onto kaolinite. *Geochim. Cosmochim. Acta.* https://doi.org/10.1016/j.gca.2004.12.029.

Ravel B. and Newville M. (2005) ATHENA, ARTEMIS, HEPHAESTUS: data analysis for X-ray absorption spectroscopy using IFEFFIT. *J. Synchrotron Rad* **12**, 537–541. https://doi.org/10.1107/S0909049505012719.

Ritchie G. S. P. and Posner A. M. (1982) The effect of pH and metal binding on the transport properties of humic acids. *J. Soil Sci.* **33**(2), 233–247. https://doi.org/10.1111/j.1365-2389.1982.tb01762.x.

Scheinost A. C., Abend S., Pandya K. and Sparks D. L. (2001) Kinetic controls on Cu and Pb sorption by ferrihydrite. *Environ. Sci. Technol.* **35**. https://doi.org/10.1021/es000107m.

Schenck C. V., Dillard J. G. and Murray J. W. (1983) Surface analysis and the adsorption of Co(ll) on goethite. *J. Colloid Interf. Sci.* **95**(2), 398–409.

Schulthess C. P. and Huang C. P. (1990) Adsorption of heavy metals by silicon and aluminum oxide surfaces on clay minerals. *Soil Sci. Soc. Am. J.* **54**, 679–688.

Schwertmann U. and Cornell R. M. (1991) *Iron Oxides in the Laboratory: Preparation and Characteristics*. VCH, Weinheim.

Sherman D. M. (2009) Surface complexation modeling: mineral fluid equilbria at the molecular scale. *Rev. Mineral. Geochem.* **70**(5), 181–205. https://doi.org/10.2138/rmg.2009.70.5.

Sherman D. M., Peacock C. L. and Hubbard C. G. (2008) Surface complexation of U(VI) on goethite (α-FeOOH). *Geochim. Cosmochim. Acta* **72**(2), 298–310. https://doi.org/10.1016/j.gca.2007.10.023.

Smith E. J., Rey-Castro C., Longworth H., Lofts S., Lawlor A. J. and Tipping E. (2004) Cation binding by acid-washed peat, interpreted with Humic Ion-Binding Model VI-FD. *Eur. J. Soil Sci.* **55**(3), 433–447. https://doi.org/10.1111/j.1365-2389.2004.00607.x.

Spark K. M., Wells J. D. and Johnson B. B. (1995) Characterizing trace metal adsorption on kaolinite. *Eur. J. Soil Sci.* **46**(4), 633–640. https://doi.org/10.1111/j.1365-2389.1995.tb01359.x.

Sparks D. L. (1995) *Environmental Soil Chemistry*. Academic Press, London.

Sposito G. (1984) *The Surface Chemistry of Soils*. Oxford University Press, New York.

Swift R. S. (1996) Organic matter characterisation. In Methods of Soil Analysis: Part 3. Chemical Methods (ed. D. L. Sparks). Soil Science Society of America, Madison, WI.

Tipping E., Griffith J. R. and Hilton J. (1983) The effect of adsorbed humic substances on the uptake of copper(II) by goethite. *Croat. Chem. Acta* **56**.

Tsutsuki K. and Kuwatsuka S. (1978) Chemical studies on soil humic acids. *Soil Sci. Plant Nutr.* **24**(4), 547–560. https://doi.org/10.1080/00380768.1978.10433134.

Webb S. M., Tebo B. M. and Bargar J. R. (2005) Structural characterization of biogenic Mn oxides produced in seawater by the marine bacillus sp. strain SG-1. *Am. Mineral.* **90**(8–9), 1342–1357. https://doi.org/10.2138/am.2005.1669.

Xia K., Bleam W. and Helmke P. A. (1997) Studies of the nature of binding sites of first row transition elements bound to aquatic and soil humic substances using X-ray absorption spectroscopy. *Geochim. Cosmochim. Acta* **61**(11), 2223–2235. https://doi.org/10.1016/S0016-7037(97)00080-X.

Yonebayashi K. and Hattori T. (1988) Chemical and biological studies on environmental humic acids. *Soil Sci. Plant Nutr.* **34**(4), 571–584. https://doi.org/10.1080/00380768.1988.10416472.

Zachara J. M., Resch C. T. and Smith S. C. (1994) Influence of humic substances on Co2+ sorption by a subsurface mineral separate and its mineralogic components. *Geochim. Cosmochim. Acta* **58**(2), 553–566. https://doi.org/10.1016/0016-7037(94)90488-X.

Zhu J., Pigna M., Cozzolino V., Caporale A. G. and Violante A. (2010) Competitive sorption of copper(II), chromium(III) and lead(II) on ferrihydrite and two organomineral complexes. *Geoderma* **159**(3–4), 409–416. https://doi.org/10.1016/j.geoderma.2010.09.006.

Associate editor: Owen Duckworth